32. Scanning Probe Studies of Nanoscale Adhesion Between Solids in the Presence of Liquids and Monolayer Films

Adhesion between solids is a ubiquitous phenomenon whose importance is magnified at the micrometer and nanometer scales, where the surface-to-volume ratio diverges as we approach the size of a single atom.

Numerous techniques for measuring adhesion at the atomic scale have been developed, but significant limitations exist. Instrumental improvements and reliable quantification are still needed. Recent studies have highlighted the unique and important effect of liquid capillaries, particularly water, at the nanometer scale. The results demonstrate that macroscopic considerations of classic meniscus theory must be modified to take into account new scaling and geometric relationships unique to the nanometer scale. More generally, a molecular scale description of wetting and capillary condensation as it applies to nanoscale interfaces is clearly desirable, but remains an important challenge.

The measurement of adhesion between self-assembled monolayers has proven to be a reliable way to probe the influence of surface chemistry and local environment on adhesion. To date, however, few of these systems have been investigated in detail quantitatively. The molecular origins of adhesion down to the single-bond level still need to be fully investigated. The most recent studies illustrate that, while new information about adhesion in these systems has been revealed, further enhancements of current techniques as well as the development of new methodologies coupled with accurate theoretical modeling are required to adequately tackle these complex measurements.

32.1 **The Importance of Adhesion at the Nanoscale** 951
32.2 **Techniques for Measuring Adhesion** 952
32.3 **Calibration of Forces, Displacements, and Tips** 957
32.3.1 Force Calibration 957
32.3.2 Probe Tip Characterization 958
32.3.3 Displacement Calibration 958
32.3.4 Cantilever Tilt 959
32.4 **The Effect of Liquid Capillaries on Adhesion** 959
32.4.1 Theoretical Background and Approximations 959
32.4.2 Experimental Studies of Capillary Formation with Scanning Probes 962
32.4.3 Theoretical Issues Revisited 964
32.4.4 Future Directions 967
32.5 **Self-Assembled Monolayers** 968
32.5.1 Adhesion at SAM Interfaces 968
32.5.2 Chemical Force Microscopy: General Methodology 968
32.5.3 Adhesion at SAM-Modified Surfaces in Liquids 969
32.5.4 Impact of Intra- and Interchain Interactions on Adhesion 970
32.5.5 Adhesion at the Single-Bond Level 972
32.5.6 Future Directions 973
32.6 **Concluding Remarks** 973
References 974

32.1 The Importance of Adhesion at the Nanoscale

The mutual attraction and bonding of two surfaces, which can occur with or without an intervening medium, are common phenomena with far-reaching manifestations and applications in society. The adherence between a raindrop and a window pane, the climbing of a gecko up a vine, the sticking of multiple adhesive note pads to a professor's wall, the force required to separate hook-and-eye (Velcro) strips, the building of a sand castle, and the book page turned by a wetted finger are all scenarios where adhesion is important. Within the complexity of these examples and others lies a central theme: that the mechanical forces between a pair of materials can be fundamentally affected by not just the macroscopic or microscopic structures of the surfaces, but also by the

interatomic and intermolecular forces that exist between them.

Adhesion and intermolecular forces have been studied for many years dating back to ancient times [32.1], and active research continues today for topics as broad as insect and reptile locomotion [32.2], interactions between cells in the body [32.3], and the design of self-healing composites [32.4], to name but a few examples. While adhesion is clearly of interest for a wide range of macroscopic applications, the importance of adhesion becomes dominant at micrometer and nanometer scales. This is primarily due to the dramatic increase in the surface-to-volume ratio of materials at these scales, an effect which renders friction and interfacial wear at such length scales critical phenomena too [32.5]. For example, the dominating effect of adhesion at this scale has affected the development of microelectromechanical systems (MEMS), where interfacial forces can prevent devices from functioning properly since the small flexible parts often emerge from the fabrication line stuck together. Studies of adhesion in MEMS are ongoing [32.6, 7], and MEMS devices that are commercially deployed rely upon sophisticated surface treatments to reduce and control adhesion [32.8–10].

Detailed control of adhesion at the molecular level will be essential for the design of even smaller nanoelectromechanical systems (NEMS). Much has been written about the possibilities for nanoscale machines, sensors, actuators, and so on. It is crucial to understand that a molecule is *all* surface, and therefore molecular and nanoscale devices cannot be properly designed, implemented, or characterized unless an understanding of atomic-scale adhesion is thoroughly presented, particularly if these devices are to involve any moving parts that will come into and out of contact. Studying adhesion at the nanoscale is important for other reasons. The protruding asperities in most MEMS materials are often nanoscale in dimension, and therefore a complete understanding of adhesion in MEMS requires investigation of the adhesive properties of the individual nanoscale asperities. In addition, the experimental study of adhesion at the nanoscale is required for the development of detailed atomic-scale models of adhesion. Such progress requires a close collaboration between experiment and theory, which is essential for the eventual success of such an endeavor.

There has been significant progress in the experimental study of adhesion at the nanometer scale using scanning probe methods, but numerous challenges exist. A discussion of solid–solid adhesion without an intervening medium is provided elsewhere in this book. This chapter focuses on how adhesion is affected by the ubiquitous presence of water, and how it can be controlled through the application of self-assembled monolayer (SAM) coatings, again in the presence of a liquid medium. In addition, we discuss specific instrumental challenges that are inherent to adhesion measurements. We do not delve into the realm of atomic-scale modeling of adhesion, nor do we discuss the role of more complex coatings such as polymer brushes and blends. Rather, our focus will be on critically evaluating the relevant experimental techniques, and critically reviewing recent results from studies of water and SAM films, which are perhaps the two most commonly encountered media in nanoscale adhesion applications.

32.2 Techniques for Measuring Adhesion

The experimental study of adhesion at the nanoscale experienced two renaissances in the previous century. The first occurred with the development of the surface forces apparatus (SFA) [32.11, 12], and the second with the later development of the AFM [32.13] and other related scanning force techniques.

SFA experiments have contributed profoundly to our understanding of adhesion. The SFA consists of a pair of atomically smooth surfaces, usually mica sheets, mounted on crossed cylinders that can be pressed together to form a controlled circular contact. The applied load, normal displacement, surface separation, contact area, and shear force (if applied) can all be controlled and/or measured [32.11, 14–16]. The SFA can be operated in air, a controlled environment, or under liquid conditions. The surfaces are often treated to attach molecules whose behavior under confinement can be studied. Alternately, the behavior of a confined fluid layer can be observed. The surface separation can be measured and controlled in the Ångstrom (Å) regime. The lateral resolution is limited to the range of several tens of micrometers. However, the true contact area between the interfaces can be directly measured, which is a key advantage since it allows an adhesive force to be converted to a force (or energy) per unit area (or per molecule), thus separating geometrical contributions to

adhesion from chemical contributions. In this chapter, we will refer to relevant results in the context of the scanning probe experiments that we discuss below. As a very brief summary, some of the most important results pertaining to adhesion include the observation of capillary effects on adhesion [32.17,18], the presence of hysteresis in adhesion due to pressure-induced restructuring of the interface [32.19], and numerous studies of how interfacial chemistry (hydrophilicity, surface charge, specific chemical groups, and so forth) affect adhesive forces [32.19–21].

AFM instrumentation is described elsewhere in this book. Significant ways in which the AFM differs from the SFA are: (1) the contact radius is nanometers, not microns, due to the fact that the tip is usually < 100 nm in radius, and the contact area at low applied loads will be a fraction of this radius [32.22]; (2) the force resolution in standard commercial AFMs is typically 10^{-10} N, and high-resolution systems have been developed that measure forces orders of magnitudes smaller, as opposed to $\approx 10^{-6}$ N with the SFA; (3) the contact area is not directly observable, which is a key disadvantage, although it may be determined or inferred by the measurement of related quantities such as contact conductance [32.23,24] or contact stiffness [32.25,26]; (4) the actual separation between the tip and sample are not directly observable, which is a key disadvantage; (5) the relative separation between the sample and the *cantilever* (not the tip) is controlled in the 0.1 nm range or better; (6) the measurement bandwidth is typically in the kHz regime, but can extend into the MHz regime depending on the data acquisition technique; (7) the operating environment includes ultrahigh vacuum (UHV), and cryogenic to elevated temperatures; (8) there is virtually no limit to the range of sample materials that can be probed by the AFM, provided the sample is not overly rough; and (9) half of the interface (the tip) is essentially unknown or uncontrolled without devoting particular effort, whereas with the SFA both surfaces are well-defined. This is another key challenge for AFM that has yet to be consistently addressed.

The general set-up of the AFM is as follows. A small sharp tip (with a radius of typically 10–100 nm) is attached to the end of a compliant cantilever (Fig. 32.1). The tip is brought in close proximity to a sample surface. Forces acting between the tip and the sample's result in deflections of the cantilever (Fig. 32.2a). The cantilever bends vertically (toward or away from the sample) in response to attractive or repulsive forces acting on the tip. The deflection of the cantilever from its equilibrium position is proportional to the normal load applied to the tip

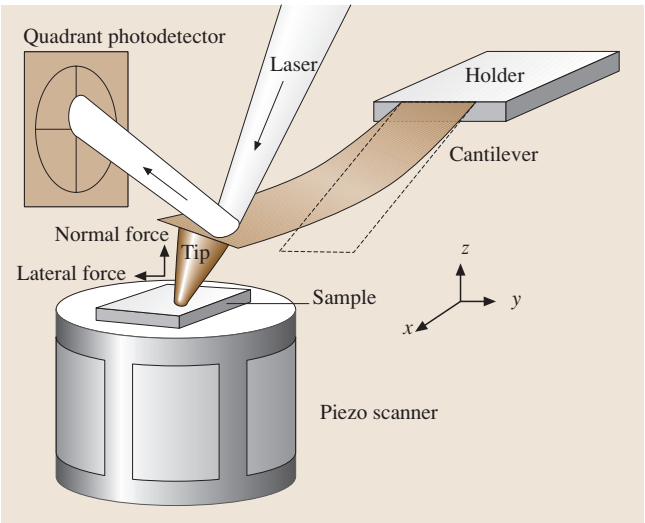

Fig. 32.1 Diagram of the AFM set-up for the optical beam deflection method. The tip is in contact with a sample surface. A laser beam is focused on the back of the cantilever and reflects into a four-quadrant photodetector. Normal forces deflect the cantilever up or down, while lateral forces twist the cantilever left and right. These deflections are simultaneously and independently measured by monitoring the deflection of the reflected laser beam

by the cantilever. Lateral forces result in a twisting of the cantilever about its long axis (torsion). These measurements can be performed in a variety of environments: ambient air, controlled atmosphere, liquids [32.27], or ultrahigh vacuum (UHV) [32.28–30].

While adhesion is often quantified in terms of a measured force, there is actually a force–displacement characteristic associated with an adhesive interface. The *work of adhesion*, as determined by fracture mechanics experiments for example, is the mechanical work per unit area needed to completely separate an interface from its initial equilibrium separation. That is, the work of adhesion is the *integral* of the interfacial force-displacement curve, normalized per unit interfacial area in contact at equilibrium. We must be careful to distinguish between the AFM tip-sample force–displacement curve and the interfacial force-displacement curve, because the former pertains to a tip on a flat surface, while the latter pertains to two flat surfaces. As we discuss in Sect. 32.5.2, if the tip radius is known it is possible to obtain the work of adhesion from an AFM pull-off force measurement.

The simplest way (perhaps deceptively so) to measure the effect of adhesion with the AFM is through so-called force–displacement plots (also referred to

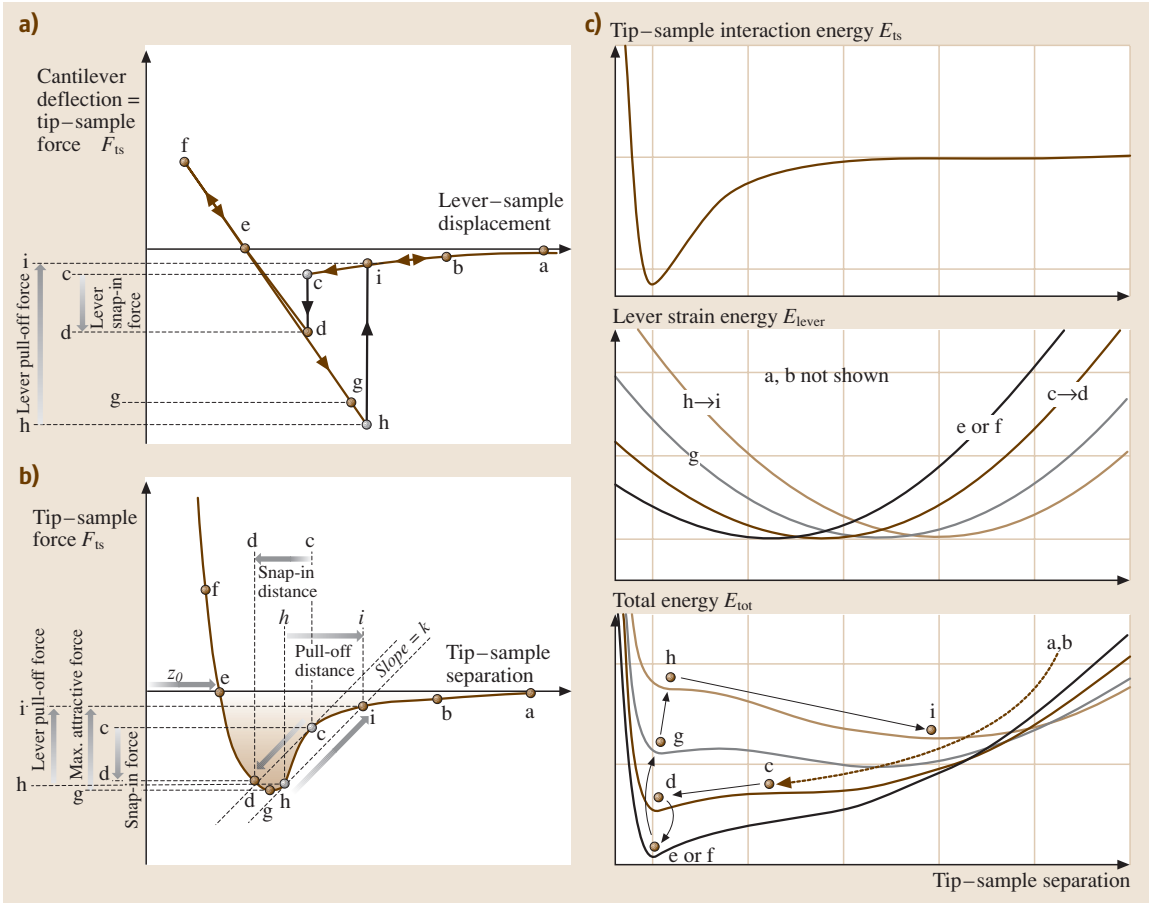

Fig. 32.2 **(a)** A "force–displacement" curve displays the vertical cantilever deflection versus the lever–sample displacement. This displacement is measured between the sample and the rigidly-held back end of the cantilever (as opposed to the front end with the tip which will bend in response to interaction forces) **(b)** The true tip–sample interaction as a function of *tip–sample* separation **(c)** Tip–sample interaction energy, lever strain energy, and total energy as a function of tip–sample separation. Note that these schematics correspond to the case of weak adhesion, when no frakture-like processes occur at the interface upon retraction. The case of strong adhesion with interfacial rupture is discussed further in the text

in the literature as force curves and force–distance curves or plots). A force-displacement plot, quite distinct from the tip-sample force-displacement curve, displays the cantilever's normal deflection versus the lever-sample displacement. The cantilever deflection can be calibrated to give the cantilever force F_{lever} (discussed further below). If we consider only the vertical forces acting on the tip to be the tip–sample interaction force F_{ts} and the cantilever force, then by force equilibrium, $F_{lever} = -F_{ts}$; in other words, these two forces are equal in magnitude. Thus, very simply, the calibrated signal from the photodiode does indeed represent the force the sample is exerting on the tip.

The lever–sample displacement is measured between the sample and the rigidly-held back end of the cantilever (as opposed to the front end with the tip, which will bend in response to interaction forces). This displacement is altered by varying the vertical position of the piezo tube which, depending on the type of AFM, displaces either the tip or the sample in the direction normal to the sample. Referring to Fig. 32.2a, the stages of acquisition of a force–displacement plot are as follows: (*a*) The lever and sample are initially far apart

and no forces act. (*b*) The lever is brought closer to the sample, and the tip senses attractive forces which cause the tip end of the lever to bend downward, thus signifying a negative (attractive) force. These forces may be of electrostatic, van der Waals, or of other origin. (*c*) At this point, the attractive force gradient (slope) of the tip–sample interaction force exceeds the normal spring constant k of the lever, and this causes an instability whereby the tip snaps into contact (*d*) with the sample. The lever–sample displacement can continue to decrease, and it eventually crosses the force axis (*e*), which corresponds to zero externally applied load. As this tip is in repulsive contact with the sample, the front end of the lever is pushed further upward, and the force corresponds to the externally applied load. (*f*) The lever-sample displacement direction is reversed at a point chosen by the user. As the lever–sample distance is reduced, the force becomes negative. Adhesion between the tip and sample maintains the contact although there is now a net negative (tensile) load. Eventually the tip passes through the point of maximum adhesion (*g*). Now the attractive force between the tip and sample starts to decrease, and so in principle the cantilever deflection will decrease. However, close to here, an unstable point is reached (*h*) where the adhesive bond ruptures. For a weak adhesive interaction, such as that due purely to van der Waals interactions in a liquid, this will occur when the cantilever stiffness exceeds the force gradient of the tip-sample interaction, and the tip snaps out of contact with the sample, as shown in (*h*)-(*i*). However, for stronger solid-solid adhesive contacts, the situation is different than that shown. The instability can be thought of as a fracture process. The rupture occurs due to high tensile stresses at the edge of the contact zone that exceed the bond strength. Therefore, pull-off will occur at (*g*). The difference in tip-sample separation between points (*g*) and (*h*) as represented in this plot is purely schematic, and in practice, fluctuations due to vibrations will cause the pull-off instability to occur before any reduction in force is observed. In any event, the resulting change in force relaxation is usually called the *pull-off force*. Note that the forces and distances are not drawn to scale; in particular, the attractive part of the interaction is exaggerated beyond that which often occurs for inert, neutral surfaces.

The cantilever force–displacement plot can be measured at a single location on the sample, or a series of measurements can be carried out over an area of interest. These so-called adhesion mapping techniques allow for spatially resolved adhesion measurements to be correlated with other sample properties such as friction, chemical termination, and other types of material heterogeneity.

To properly derive information about the tip-sample adhesion force from the AFM, it is critical to understand the nature of the mechanical instability in both snap-in and pull-off processes. The fundamental point to comprehend is that *the pull-off force is not the adhesive bond strength*. In other words, *it is not a direct measure of the actual adhesive forces that were acting between the tip and sample in the absence of applied load.* This important point is often overlooked or misunderstood, and so we discuss it in some detail here.

A cartoon of the interaction force F_{ts} between the tip and sample is sketched (not to any particular scale) as a function of the true tip–sample separation in Fig. 32.2b. Superimposed on this is the force–distance relation of the cantilever: a straight line with slope k (N/m), the cantilever stiffness (diagonal dashed lines). Points of instability are shown as gray dots, labels and arrows, as opposed to stable points shown as black dots, labels, and arrows. Snap-in occurs when the attractive force gradient $\mathrm{d}F_{ts}/\mathrm{d}z$ just exceeds k; in other words, when the dashed line is tangent to the tip–sample force curve, as shown for point (*c*). This instability is a direct consequence of Newton's Second Law and is explained further below. Similarly, the pull-off occurs when during retraction k finally just exceeds $\mathrm{d}F_{ts}/\mathrm{d}z$, as shown for point (*h*), where once again, the diagonal line is just tangent to the tip–sample force curve. By definition, since k is finite, this point *cannot* correspond to the point of maximum attractive force (or adhesive force), (*g*). Thus, the force at which pull-off occurs is *not* precisely equal to the true adhesion force. How significant this deviation will be is discussed below.

This can also be illustrated from an energetic perspective. In Fig. 32.2c, we show separately the tip–sample interaction energy, E_{ts}, as a function of tip–sample separation (top), followed by the quadratic elastic strain energy, E_{lever}, of the cantilever (middle) and the sum, E_{total}, of the two (bottom). As the lever–sample displacement is varied, the elastic energy curve is shifted to the appropriate position which, for this example, is represented on the tip–sample separation axis. Far away from the sample, the system resides in a deep minimum (points (*a*) and (*b*), not shown). As the tip–sample separation is reduced, this minimum becomes increasingly shallow (evolving along the dashed arrow). At the snap-in point (*c*) the minimum is eliminated since the attractive energy of the tip–sample interaction has overwhelmed the energy minimum of the cantilever. Mathematically, this is described as an inflection point,

where:

$$\frac{\mathrm{d}^2 E_{\mathrm{tot}}}{\mathrm{d}z^2} = 0\,. \tag{32.1a}$$

The total energy is given by

$$\begin{aligned} E_{\mathrm{tot}} &= E_{\mathrm{ts}} + E_{\mathrm{lever}} \\ &= E_{\mathrm{ts}} + \frac{1}{2}k(z - z_0)^2 \end{aligned} \tag{32.1b}$$

Therefore, snap-in occurs when

$$\frac{\mathrm{d}^2 E_{\mathrm{ts}}}{\mathrm{d}z^2} = -\frac{\mathrm{d}F_{\mathrm{ts}}}{\mathrm{d}z} = -k\,. \tag{32.1c}$$

This explains why the instability is described by the line of slope k being tangent to the tip–sample force curve as shown in Fig. 32.2b. The system now dynamically finds the new minimum, by following the gray arrow to point d where a mechanical contact between the tip and sample is now formed. There will, of course, be dynamics associated with this transition which can result in a damped oscillation as the system settles into its new stable equilibrium.

Note that once the contact is formed, the tip and sample elastically deform and so, strictly speaking, the tip–sample potential will be distinct from the potential shown before contact occurs. For simplicity we have left out this change, and instead have drawn the potential as a single-valued function. However, such changes in the energy landscape should be considered in a complete description of the problem [32.31].

Nevertheless, it will also hold true that upon retracting the tip from the surface, the stable minimum seen at (e), (f), and then (g) becomes more shallow and eventually disappears as it is overwhelmed by the strain energy of the cantilever. Again, an inflection point is created when:

$$\frac{\mathrm{d}^2 E_{\mathrm{ts}}}{\mathrm{d}z^2} = -k\,, \tag{32.2}$$

in other words, when again

$$\frac{\mathrm{d}F_{\mathrm{ts}}}{\mathrm{d}z} = k\,. \tag{32.3}$$

This second instability occurs at point (h), the pull-off point. The system then follows the gray arrow to point (i), where the tip is now out of contact with the sample (but experiencing a small amount of attractive force due to whatever long-range attractive forces exist).

If the spring is sufficiently compliant (low k), or the potential sufficiently curved (large $\frac{\mathrm{d}F_{\mathrm{ts}}}{\mathrm{d}z}$ shortly past the minimum at (g)), and if the long-range attractive force at (i) is small, then the pull-off force *does* nearly correspond to the *maximum attractive force*, as indicated in Fig. 32.2b. In other words, point (h) would occur very close to point (g), and point (i) is close to a force of zero. The value of the force at (i) can be determined by retracting the cantilever sufficiently far from the surface, which is often practical except for strong, long-range forces that may occur, for example, when charge is present on the surface or the tip. Of more fundamental concern is that if the cantilever is somewhat stiff, or if the potential is rather compliant (which may be the case for organic, polymeric, biological or liquid systems), then the pull-off force may differ substantially from the maximum attractive force. For such cases, the distinction between the pull-off force and the maximum attractive force is important, and the limitations imposed by the AFM's intrinsic instabilities become apparent. Of course, if a cantilever with a stiffness that exceeds the attractive force gradient at all points is used, one will avoid the instabilities. However, since it is the deflection of the cantilever that is used to sense the force, one would have to trade off force sensitivity with stability, which is often an unwanted compromise.

In addition, the discussion above is entirely predicated upon the notion that there is a unique (i. e. non-hysteretic) force-displacement interaction between the tip and sample. In fact, as mentioned above, local rupture of adhesive bonds between the tip and the sample during retraction can occur because of the high tensile stresses. Therefore, for the same tip position, more than one metastable configuration of the atoms is possible. One case could be where the atoms have separated, and only weak van der Waals interactions occur. Another case would be where the atoms remain chemically bonded and strained in tension. The rupture of the tip-sample contact will occur instead at or very close to point (g) in Figs. 32.2a and 32.2b, regardless of the spring constant of the cantilever.

When a compliant spring or holder is used to manipulate a probe, as is the case for AFM, the technique is generally referred to as being "load-controlled", since the load can be prescribed, but the actual displacement of the probe with respect to the sample cannot (as illustrated by the jump in displacement that occurs during snap-in or pull-off).

In contrast, "displacement-controlled" techniques avoid this instability by effectively eliminating the compliance of the spring, thereby directly probing the tip-sample interaction. This has been carried out for decades in the mechanical testing community, and displacement-controlled scanning probes have been developed over the past ten years. This is accomplished by displacing the tip by direct application of a force

to the tip itself. Pethica and coworkers [32.32, 33] use a magnetic coating on the tip and external coils to apply forces to the tip. They refer to the instrument as a "force-controlled microscope". *Houston* and coworkers [32.34, 35] control the force electrostatically and refer to the instrument as an "interfacial force microscope" (IFM). Lieber and coworkers use a variation on Pethica's method, where a magnetic coil is used to apply a force to the cantilever [32.36], and adapted it to work in solution.

An example of an adhesion measurement with the IFM is shown in [32.37], which shows that the instrument is able to measure the entire interaction force curve without instabilities. Thus, this provides a *direct* measurement of the minimum interaction force (as well as forces at all other tip–sample separations) and is a more reliable measure of adhesion. The disadvantage with these techniques is primarily one of inconvenience: the probes require extra manufacturing steps and control electronics. However, given the importance of adhesion in nanoscale science and technology, the extra information gained makes these techniques clearly worth the effort.

Pull-off instabilities can occur even in a displacement-controlled experiment. In this case, the instability is an "intrinsic" instability whereby the adhesive force gradient competes with the stiffness of the *contact itself* [32.38, 39]. Adhesive materials with low stiffness, such as polymers, may show this behavior.

Another way to avoid these instabilities while maintaining, or in fact, enhancing the force sensitivity, is to use dynamic AFM techniques [32.40]. In this case, the inertia of the cantilever, driven at or near its resonance, prevents the instabilities from occurring. The resonance frequency shift of the cantilever is sensitively measured, and this can be related to the integral of the force the tip experiences during its oscillation cycle. Thus, the force–displacement curve is mapped out by interpolating the data [32.41]. Uncertainty can be introduced by the interpolation scheme, since significant attraction is only experienced at the very bottom of the tip's oscillation cycle. Using small oscillations with high sensitivity force detection avoids this difficulty [32.42].

Finally, the pull-off force may show a time dependence that arises from intrinsic viscoelasticity of the tip or sample materials [32.43], or kinetic effects due to adsorption or reaction of materials at the interface [32.44]. These regimes remain relatively unexplored but certainly, to compare adhesion measurements between labs, the velocity of approach and retraction, as well as the time in contact, ought to be reported for any published experimental results.

A quantitative and reliable examination of adhesion therefore requires careful consideration of the mechanics of the contact and the cantilever. For an AFM experiment where instabilities occur, one can conclude that the pull-off force is a good measure of adhesion only if (1) the materials are fully elastic with little or no viscoelastic character, (2) the interface is chemically stable, (3) the cantilever stiffness is sufficiently low compared with the adhesive force gradient, and (4) the contact stiffness is sufficiently high compared with the adhesive force gradient. Otherwise, a more thorough investigation is required.

32.3 Calibration of Forces, Displacements, and Tips

Whether the forces are to be measured with load-controlled or displacement-controlled techniques, measurements cannot be compared between laboratories unless the forces are properly calibrated. Unfortunately this can be a rather involved task, and adoption of standards has yet to become widespread and robust. Here we provide a summary of the pertinent issues with references to other works for further reading; these issues are also discussed elsewhere in this book.

32.3.1 Force Calibration

Commercially available AFM cantilevers often come in two common forms: V-shaped and rectangular. Silicon and silicon nitride are the typical materials, but other choices are becoming popular. Reflective coatings are often applied to enhance the reflectivity to collect more laser light in the photodiode. The normal force constant of a monolithic rectangular cantilever beam requires knowledge of all lever dimensions and its modulus [32.45]. For a rectangular beam of length L, width w, thickness t and Young's modulus E, the normal bending stiffness k is given by:

$$k = \frac{Ewt^3}{4L^3} \,. \tag{32.4}$$

The cubic dependence on thickness is particularly problematic since in microfabrication processes t is usually determined by etching processes that are not precisely controlled, and the thickness is difficult and cumber-

some to measure experimentally. Variations in E can also occur depending on the type of cantilever, particularly for silicon nitride cantilevers, although the dependence on E is clearly not as critical. If a bulk value for E is used, the thickness can be determined by measuring the resonance frequency of the cantilever [32.46]. However, this method only works for uncoated monolithic cantilevers, since the metal coatings applied to enhance reflectivity or for other purposes will also alter the spring constant substantially [32.47]. In addition, formulae for V-shaped levers are substantially more complicated. Uncoated, single-crystal silicon cantilevers are perhaps the only ones for which the force constant can be reliably determined by using (32.4) and the resonance frequency [32.48]. Otherwise, an experimental, preferably in situ, calibration method is strongly encouraged.

Experimental methods used to calibrate the force constant of AFM cantilevers have been extensively discussed [32.46,49–59]. It has been repeatedly shown that the manufacturer's quoted spring constants can be in error by large factors and should not be used in any quantitative research effort. We will not delve into the details of these calibration methods, but we do make note of one particularly recent method proposed by *Sader* et al. [32.60] which appears to be reliable and simple to perform for rectangular levers. It relies on measuring the resonance frequency and the quality factor of the cantilever in air. Use of the hydrodynamic function relates the damping effect of air to the quality factor and resonance frequency, and the dependences on E and t are eliminated from the resulting formula for the force constant. The measurement and calibration method can be carried out in a matter of minutes, particularly if the AFM software can find the resonance and then calculate the quality factor and resonance frequency. Care should be taken to account for background signal and filtering by the detection instrumentation at high frequencies.

32.3.2 Probe Tip Characterization

A problem of quite a different nature is that the geometry of the contact formed between the AFM tip and sample surface is not defined if the tip shape and composition is not known. This issue is of crucial importance since one is trying to understand the properties of an *interface*, and the tip is half of that interface.

The adhesion force between the tip and sample is a meaningless quantity in the absence of any knowledge of the tip shape [32.22]. The only use for such measurements is in cases where the *same* tip is used to compare different samples or different conditions, and verification by cyclic repetition of the experiments is carried out to ensure that the tip itself did not change during the experiment.

There are several in situ methods that are used to characterize the tip shape. A topographic AFM image is actually a convolution of the tip and the sample geometry [32.61]. Separation of the tip and sample contributions by contact imaging of known, or at least sharp, sample features allows the tip shape to be determined to a significant extent [32.62–73]. Ex situ tip imaging by transmission electron microscopy has also been performed and can produce images with nanometer-scale resolution [32.72,74]. Some of these measurements have revealed that a large fraction of microfabricated cantilevers possess double tips and other unsuitable tip structures [32.63, 67, 73]. This convincingly demonstrates that tip characterization is absolutely necessary for useful nanotribological measurements with AFM. Thin film coatings applied to the microfabricated levers can provide robust, smooth and even conductive coatings [32.74–76]. Further work in this direction would be useful, so as to provide a wider array of dependable tip structures and materials.

In addition to the shape of the tip, the chemical composition of the tip is equally important, but is also challenging to determine or control. *Xiao* and coworkers have shown that the AFM tip is readily chemically modified when scanned in contact with various materials [32.77], even tips that have been coated with self-assembled monolayers in order to control their chemistry. They recommend "running in" the tip with a standard sample to give reproducible results. The stresses that take place in a nanocontact can be very large [32.5], and so modification of both the chemistry and structure of the tip is important to consider.

One class of experiments where the tip shape and chemistry is not as critical is in cases where a molecule or nanostructure is tethered to the end of the tip and specific interactions are probed [32.78–82]. Another alternative method is to use colloid probes [32.83, 84], whereby colloidal particles are attached to the cantilever on top of (or in place of) the tip. This method requires a unique calibration procedure [32.85], but provides particles whose structure and chemistry can be measured and perhaps controlled prior to attachment to the lever. The nanoscale roughness of these probes does need to be considered carefully though, as it will affect the interfacial properties.

32.3.3 Displacement Calibration

Proper signal and spatial calibration also requires knowledge of the sensitivity of the piezoelectric scanning elements. This can involve complications due to instrumental drift [32.87] and inherent piezoelectric effects, namely nonlinearity, hysteresis, creep, and variations of sensitivity with applied voltage [32.88–92]. Caution must be exercised when determining and relying upon these parameters. Techniques such as laser interferometry [32.93], scanning sloped samples [32.53, 89], scanning known surface step heights [32.94] or the use of precalibrated piezoelectrics [32.95] can facilitate piezo calibration.

32.3.4 Cantilever Tilt

One final issue of concern is that the cantilever itself is tilted by typically 10–20 °C in most AFMs (Fig. 32.3). This is to ensure that the tip makes contact with the sample before any other component, such as the nearby sides of the cantilever chip, but it introduces coupling between the mechanical forces of interest. Consider an experiment where the load is varied by moving the fixed end of the lever relative to the sample along the z-axis. Because of the tilt, the tip end of the lever displaces in the x-direction in Fig. 32.3b. Thus, with increasing load (with decreasing separation between the fixed end of the lever and the sample surface), the tip end of the lever moves in the $+x$-direction. Similarly, the tip retraces this path when the lever retracts from the surface. This issue was highlighted some time ago by *Overney* et al. who discussed the effect of in-plane displacement on elastic compliance measurements and accounted for it in their experiments [32.96]. In addition, *Marcus* et al. and *D'Amato* et al. addressed consequences of the tilt angle in AFM in relation to phase contrast imaging in intermittent-contact AFM [32.97, 98], and *Cannara* et al. [32.86] discussed a methodology for correcting the effect when acquiring friction measurements. Both *Overney* et al. and *Cannara* et al. propose moving the fixed end of the lever relative to the sample along the z'-axis shown in Fig. 32.3b, instead of the z-axis. This is also useful for adhesion measurements, as it will restrict the range of motion of the tip across the sample as the load is varied.

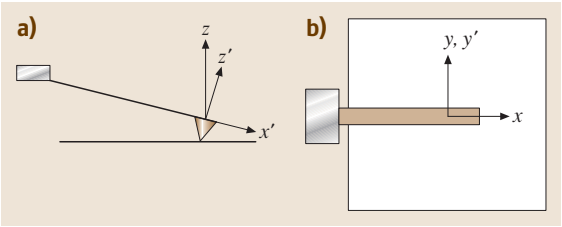

Fig. 32.3 (**a**) *Side view* and (**b**) *top view* of the lever–sample system in an atomic force microscope. The x-axis corresponds to the projection of the cantilever onto the sample surface. Tip displacement (or motion of the tip end of the lever) versus load occurs along this axis. Load is varied by moving the fixed end of the lever relative to the sample along the z-axis. After [32.86]

Heim et al. [32.99] pointed out that pull-off forces or any other measured normal force needs to be corrected for the effect of tilt. They propose a specific correction factor and show that the correction can be as large as 20-30% for tilt angles of 20°. *Hutter* [32.100] has proposed a modification to their equation. Note that issues of tilt are absent for the IFM described above, since the tip and force sensor are oriented directly normal to the sample surface.

32.4 The Effect of Liquid Capillaries on Adhesion

32.4.1 Theoretical Background and Approximations

The adsorption of water and other liquids onto surfaces, and their subsequent behavior at interfaces, continues to be a vibrant area of research. The importance of liquid–solid interface behavior is massive, encompassing topics as broad as paints, textiles, lubricants, geology and environmental chemistry, and covering all corners of biology.

The ability to measure forces at the nanoscale using scanning probe microscopy has generated much interest in these fields. For any force measurement carried out in ambient laboratory conditions, the possibility of a capillary neck forming between the tip and sample must be considered. The study of such necks may in turn provide insight into the behavior of the liquid, which is discussed in other chapters in this book. In order to provide background for these emerging areas, we consider here the fundamen-

tal mechanical and chemical aspects of adhesion in the presence of a liquid meniscus. By way of introduction, *Israelachvili* [32.1] and *de Gennes* [32.101] provide rigorous coverage of the terminology, physics, and chemistry of liquid films and their wetting properties.

Water readily adsorbs at many surfaces. At a crack or sharp corner, it can condense to form a meniscus if its contact angle is sufficiently small. The small gap between an AFM tip and a surface is therefore an ideal occasion for such condensation. Early on it was realized that liquid condensation plays a significant role in tip–sample interactions [32.103, 104].

The AFM literature has so far idealized the tip as a sphere of radius R and applied the classic theory of capillary condensation between a sphere and a plane, which as based on the thermodynamics of capillary formation. Within this theory, geometrical assumptions are often made. In particular, when the radius of the sphere is large with respect to the size of the capillary, one possible approximation is known as the "circle approximation", in which the meniscus radii of curvature are taken to be constant. The geometry of the capillary meniscus using the circle approximation is shown in Fig. 32.4, which is adapted from [32.102]. Hydrophobic surfaces are sketched on the left half ($r_1 > 0$), and hydrophilic surfaces sketched on the right half ($r_1 < 0$).The water contact angles with the sample and tip respectively are θ_1 and θ_2. D represents the separation of the tip and sample. The angle ϕ is referred to as the "filling angle". The pressure difference, or Laplace pressure, across a curved interface is given by the Young–Laplace equation [32.1, 102]:

$$\Delta p = \gamma \left(\frac{1}{r_1} + \frac{1}{r_2} \right) \tag{32.5}$$

where r_1 and r_2 are defined in Fig. 32.4 and γ is the surface tension of the liquid, which in this case is water. The resulting force is attractive if $\Delta p < 0$. Note that $r_1 > 0$ and $r_2 < 0$. If the capillary formation is isothermal, then one can derive the Kelvin equation:

$$R_M T \ln \left(\frac{p}{p_0} \right) = \gamma V \left(\frac{1}{r_1} + \frac{1}{r_2} \right) , \tag{32.6}$$

where p_0 is the saturation pressure of the liquid, V is the molar volume of the liquid, T is the temperature, and R_M the molar gas constant. The ratio p/p_0 simply corresponds to the relative vapor pressure of the liquid, which in the case of water is just the relative humidity (RH). This is often rewritten in terms of the Kelvin radius r_K:

$$r_K^{-1} = \left(\frac{1}{r_1} + \frac{1}{r_2} \right) = \frac{R_M T}{\gamma V} \ln \left(\frac{p}{p_0} \right) . \tag{32.7}$$

The Kelvin radius varies logarithmically with the partial pressure of the liquid and is by definition less than zero (negative values correspond to convex curvature). For water at 20 °C, $\gamma V / R_M T = 0.54$ nm. A graph of r_K versus p/p_0 is shown in Fig. 32.5. Of particular note is the fact that starting from $p/p_0 = 0.75$ and lower, we find that $|r_K| < 2$ nm. Although widely used, Eqs. (32.5–32.7) are approximate because r_1 and r_2 are not normal everywhere to the meniscus surface and hence the assumed meniscus shape is not isobaric. This point will be elaborated in Sect. 32.4.3.

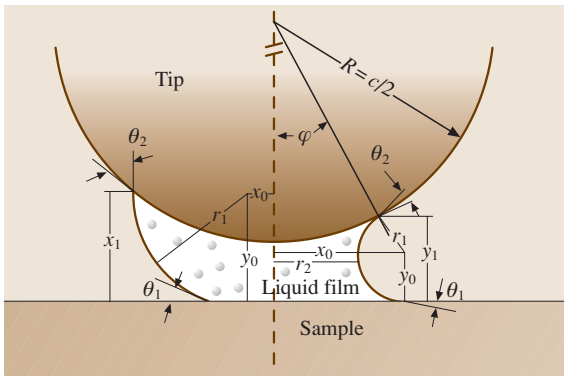

Fig. 32.4 The AFM tip, considered as a sphere at a distance D from the sample. The liquid film in-between may form a concave (*right*) or convex (*left*) meniscus in the plane shown. Figure is based on [32.102] but with significant changes

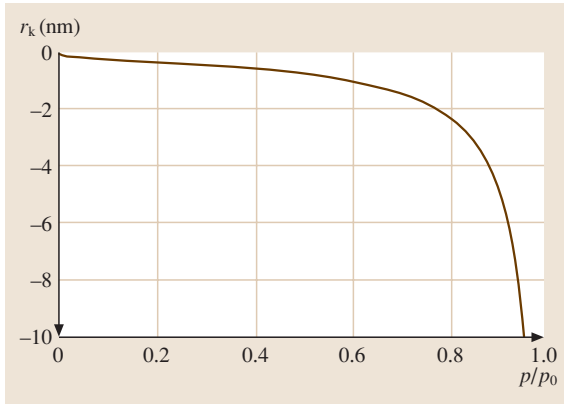

Fig. 32.5 The Kelvin radius of water at 20 °C plotted as a function of the relative humidity

A simple equation for the maximum attractive capillary force F_c between the tip and sample that is commonly used is

$$F_c = -4\pi\gamma R\cos\theta. \tag{32.8}$$

This equation is calculated by considering the Laplace pressure only. The adhesion force is predicted to be independent of RH. Notice that an immediate problem arises, which is that it predicts a finite force even at 0% RH, where there can be no capillary formation. Derivations of (32.8) are presented in several other publications [32.1, 102, 105, 106]. Significantly, this equation and its use with AFM experiments contains several assumptions, *many of which may not be valid for an AFM experiment*:

1. $|r_1| \ll R$, which is equivalent to saying ϕ is small;
2. $|r_1| \ll |r_2|$;
3. $\theta_1 = \theta_2$;
4. $D \ll |r_1|$, $|r_2|$;
5. The tip is shaped like a perfect sphere.;
6. The effect of solid–solid adhesion is negligible with respect to the meniscus force;
7. The meniscus cross-sections are perfect circular arcs;
8. The force from the Laplace pressure dominates the force due to the resolved surface tension of the meniscus;
9. The surface tension γ is independent of the meniscus size;
10. The meniscus volume remains constant as the tip is retracted;
11. The maximum force of attraction is equal to the pull-off force;
12. The tip and sample are perfectly rigid.

Assumption (1) may not be true, since the tip radius may indeed be small and comparable to the meniscus curvature radii. Assumption (2) may not be true since the small tip geometry may cause the two meniscus curvature radii to be similar. Assumption (3) is by no means true if the tip and sample are made of different materials. Assumption (4) may not be true, since both the separation of the tip and sample as well as the radii r_1 and r_2 may be in the nanometer range. Assumption (5) may be slightly or grossly in error, and is a particularly dubious assumption in the absence of tip characterization. Also, for large menisci, the capillary will grow beyond the end of the tip and start climbing up its shank which may be pyramidal or conical in shape. Assumption (6) may also be inaccurate if van der Waals or other adhesive forces are significant, and this is discussed further in the next section. Assumption (7) is not correct [32.106], and the regimes where it is a reasonable approximation require close scrutiny. Assumption (8) will be inaccurate at high relative vapor pressures [32.1, 105]. The nature of assumptions (1)-(8), and corrections to the theory to account for their violation, are presented in the work of *Orr* and *Scriven* [32.106]. This theory remains within the bounds of the classical picture of capillary formation. Results from numerical calculations in which this theory is applied are given later in this section. It will be seen that for (32.8) the geometrical assumptions alone do not severely restrict it.

Assumption (9) concerns an important scientific question that has not been fully resolved and represents the possible violation of the classical framework by molecular effects at the nanoscale. SFA measurements by *Israelachvili* have indicated that for cyclohexane and other inert organic liquids, γ remains nearly equal to its macroscopic value even for Kelvin radii that, remarkably, correspond to one or two molecular diameters. However, for water, the adhesion force comes to within 10% of the bulk prediction only for $p/p_0 > 0.9$, which corresponds to Kelvin radii greater than ≈ 5 nm in magnitude [32.17]. Later, Christenson [32.107] improved the symmetry of the SFA leaf spring and found that (32.8) holds for cyclohexane, n-hexane and water for $p/p_0 > 0.7$. Nonetheless, these deviations from macroscopic thermodynamic predictions alone calls the use of (32.8) into serious question for AFM measurements. Rather, the exploration of this deviation at the molecular scale presents a unique opportunity for scanning probe measurements.

Assumptions (10) and (11) are not assumptions of (32.8) itself, but rather assumptions that are often used when applying (32.8) to AFM measurements. Equation (32.8) simply gives the maximum force of attraction between the tip and sample. As discussed above, an AFM does *not* measure this quantity. Rather, it measures the force at which an instability occurs. If a capillary has formed between the tip and sample, then the force as a function of distance can be calculated. Calculating this force requires making one of two assumptions: either the volume of the capillary is conserved (due to the rate of displacement being large with respect to the adsorption or desorption kinetics of the liquid) or the Kelvin radius is conserved (the rate of displacement is slow with respect to the adsorption or desorption kinetics of the liquid, and so the capillary remains in equilibrium). The constant volume assumption (10) has been used in every paper we have reviewed. *Israelachvili*, however, pointed out the difference between these two approaches in his

book [32.1], and left the solution of the problem as an exercise to the reader. The force is the same at $D = 0$, but the reduction in force with displacement is more rapid and linear for the constant Kelvin radius case. With the assumptions listed above for the constant volume case

$$F(D) = 4\pi R\gamma_l \cos\theta \left(1 - \frac{D}{\sqrt{4r_K^2 \cos^2\theta + D^2}}\right), \quad (32.9)$$

while for the constant Kelvin radius case,

$$F(D) = 4\pi R\gamma_l \cos\theta \left(1 - \frac{D}{2|r_K| \cos\theta}\right). \quad (32.10)$$

As with the problem of scale-dependent surface tension mentioned above, the kinetics of capillary formation and dissolution is a relatively unexplored problem and is therefore worthy of further investigation. A recent study of the humidity dependence of friction as a function of sliding speed is an example where this issue is raised [32.108].

Once an assumption about how the meniscus changes with displacement has been made, one still needs to consider the nature of the instability in order to relate the AFM pull-off measurement to the capillary's properties. As stated above and shown in Fig. 32.2, a low lever stiffness k or a strongly varying adhesive force will lead to a pull-off force that is nearly equal to the adhesive force, and so assumption (11) would be valid. However, if k is sufficiently large, or the capillary stiffness sufficiently weak, this assumption will fail. As we shall see below, experimental efforts to investigate this point are yet to be carried out.

Finally, assumption (12), if violated, requires a substantially more complex analysis to deal with it. The question has been addressed independently by *Maugis* [32.109] and *Fogden* and *White* [32.110]. Both papers provide a nondimensional parameter that allows one to determine the severity of the effect. In the limit of small tips, stiff materials, large (in magnitude) Kelvin radii, and low surface tensions, the effect of elastic deformation is negligible. However, for relatively compliant materials, large tips, and small Kelvin radii, the meniscus can appreciably deform the contact in the immediate vicinity of the meniscus. This can substantially alter the mechanics of adhesion as well as significantly affecting the stresses. The dependence on the Kelvin radius is particularly critical. This effect may be of particular concern with soft materials like polymers or biological specimens. According to *Maugis*, the problem becomes analogous to the adhesive contact problem for solids, discussed by *Johnson* et al. [32.111], and further studied in many papers since [32.31, 112, 113].

32.4.2 Experimental Studies of Capillary Formation with Scanning Probes

There have been several experimental and theoretical investigations of how pull-off forces are affected by liquid capillaries. These studies have mostly focused on the effect of relative humidity. We do not present an exhaustive review here, but rather we summarize a few key results that highlight the important trends observed and the outstanding questions that remain.

Early on, it was realized that water capillary formation occurred readily if at least one of the two surfaces in contact was hydrophilic. Higher adhesion will lead to higher contact forces and therefore larger elastic contact areas, and this can degrade the lateral spatial resolution of the AFM, as was observed by *Thundat* and coworkers [32.114]. Furthermore, several observations have confirmed the expected result that capillary formation was readily prevented for hydrophobic surfaces. For example, *Binggeli* and *Mate* [32.104, 115] showed that tungsten tips in contact with clean silicon wafers with a hydrophilic native oxide exhibited strong adhesion and long pull-off lengths, whereas surfaces treated with a hydrophobic perfluoropolyether (such as Z-DOL) showed pull-off forces reduced by a factor of 2–3. These results were confirmed by *Bhushan* and *Sundararajan* [32.116],

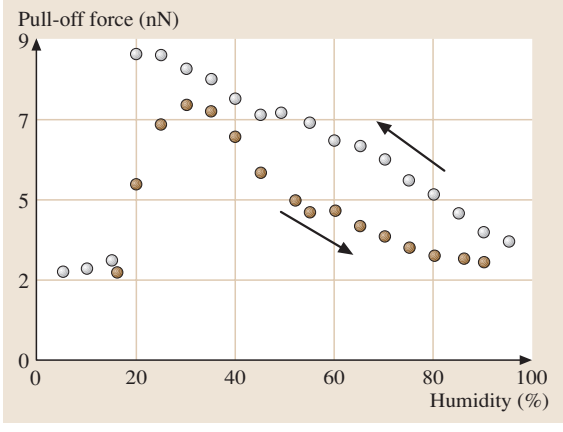

Fig. 32.6 Pull-off force between a silicon nitride tip and the muscovite mica surface as a function of RH. Two sets of data are shown; increasing (*open circles*) and decreasing (*closed circles*) humidity. After [32.44]

who investigated the pull-off force between silicon nitride tips and Si(100) with and without Z-DOL coatings for a range of relative humidities. As another example, MoO_3 films, likely hydrophilic, showed a sixfold increase in pull-off force measured with silicon tips from 0 to 50% RH [32.117].

While these examples illustrate some basic trends, the need for more finely resolved measurements as a function of humidity has been addressed only quite recently. For example, *Xu* et al. measured adhesion between a silicon nitride tip and (hydrophilic) muscovite mica in $\approx 5\%$ RH increments. The result is shown in Fig. 32.6. There are three identifiable regions: constant adhesion at low RH (<20%), increasing adhesion, and then decreasing adhesion. Some hysteresis is seen between experiments conducted with increasing and decreasing RH, but the overall trend is preserved. *Xu* et al. correlated their measurements with detailed studies of the growth of molecular water films on the mica surface which they could image directly using scanning polarization force microscopy (Fig. 32.7). They proposed that below 20%, capillary condensation does not occur, and indeed, they see no evidence of a water film at these low humidities. Above 20% RH, a strongly bound molecular water layer is formed on the bare mica surface (Fig. 32.7). In the presence of the tip, a capillary meniscus can condense. Above 40% RH, the pull-off force decreases. Recognizing one of the limitations of (32.8), they attribute this to the violation of assumption (5) listed above. They argue that for a pyramidal AFM tip, r_1 and r_2 become comparable in magnitude (and remain opposite in sign) once the capillary reaches the shank of the tip, leading to a near cancellation of the Laplace pressure given in (32.5). This argument is certainly plausible, although a rigorous proof is not provided, and the other limitations of (32.8) are not discussed in relation to this issue. Nevertheless, the correlation between the onset of adhesion increase and the formation of the molecular water film as seen directly in their dramatic images is an extremely convincing case where the classical assumptions of (32.8) must be modified to account for the molecular structure of the water film.

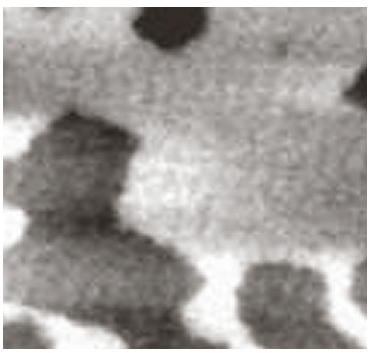

Fig. 32.7 Scanning polarization force microscopy image of water structures on the muscovite mica surface. A degree of polygonal shape to the boundaries can be seen. The signal represents two distinct phases of water that are present as a molecular film below 45% RH After [32.44]

Further considerations of the limitations of (32.8) were measured, discussed, and modeled in a detailed paper by *Xiao* and *Qian* [32.105]. Adhesion measurements, collected in large numbers for good statistics, were carried out with the same silicon nitride tip on two different surfaces: hydrophilic SiO_2, and a hydrophobic layer of *n*-octadecyltrimethoxysilane (OTE) on SiO_2. Contact angle measurements to confirm the assertion of hydrophilicity were not presented; however, the OTE surface was confirmed to be hydrophobic with a water contact angle of 108°. The results are shown in Fig. 32.8. The hydrophobic surface shows no dependence on RH, whereas the hydrophilic bare SiO_2 surface shows three regimes similar to the result of *Xu* et al.: constant pull-off force ($\gtrsim$30% RH), increasing pull-off force (30%–70% RH) and then decreasing pull-off force. *Xiao* and *Qian* discuss the limitations of (32.8) in substantial detail. In particular, they consider the violation of assumptions (1) through (8) listed above. This includes a treatment of van der Waals adhesion, with the effect of electrostatic screening of this force by the water itself taken into consideration. Equations for this more general case are presented. With all these aspects taken into account, they are only able to fit the model to their data qualitatively (Fig. 32.9). At low RH (< 10%), the van der Waals force dominates and the adhesion is initially constant. At intermediate values, the Laplace pressure contribution increases and then begins to saturate. The contribution from the resolved surface tension becomes significant at high RH (above $\approx 80\%$), and the contribution from the Laplace pressure begins to drop strongly around this same point. It should be noted that their capillary model still assumes constant values of r_1 and r_2 for the entire meniscus, and while it may be an improvement on (32.8), it is not precise. Qualitatively, this reproduces their results (and the aforementioned ones) by producing regimes of constant, increasing, then decreasing adhesion. However, the humidities at which the transitions occur, and the relative changes in adhesion, do not match the data. Somewhat better agreement at high RH (> 70%) is found by considering alternate (blunt) tip

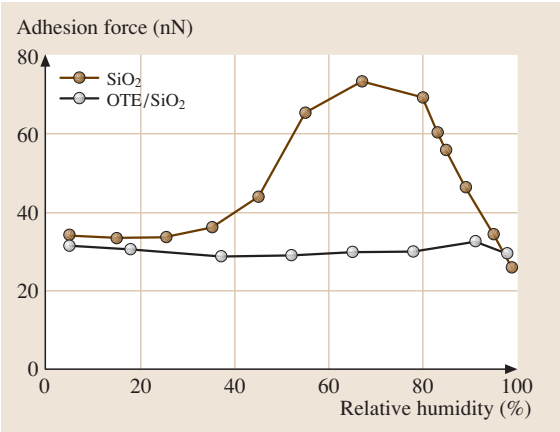

Fig. 32.8 Pull-off force as a function of RH for adhesion between a silicon nitride tip and SiO_2 (*filled circles*) and OTE/SiO_2 (*open circles*) samples. After [32.105]

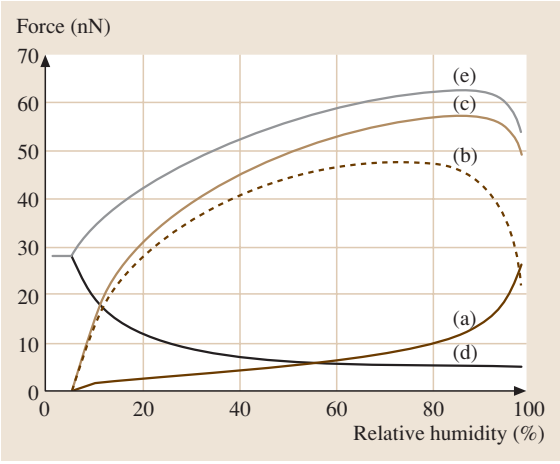

Fig. 32.9a–e Contributions to the adhesion force as a function of humidity: **(a)** resolved surface tension force; **(b)** Laplace pressure force; **(c)** total capillary force (Laplace + surface tension); **(d)** van der Waals force; **(e)** total adhesion force. After [32.105]

shapes. Nevertheless, the most significant discrepancy occurs for low RH, where the extent of the constant adhesion force is underestimated by the classical theory. The authors attribute this to a failure of the classical continuum theory to properly describe the properties of a molecular-scale meniscus, as earlier concluded using the SFA [32.107]. Another interesting point of this study is that at low RH, the adhesion is very similar for both samples, a fact which the authors attribute to the dominance of the van der Waals force for both samples (which is largely determined by the substrate and not affected significantly by the OTE film).

Slightly more recently, *He* et al. have studied capillary forces for a variety of tip–sample pairs [32.118]. Hydrophilic tips (silicon and silicon nitride with no surface treatment) and hydrophobic tips (coated with *n*−octadecyltrichlorosilane) were used. The hydrophobic character of the tip was asserted based on a water contact angle measurement of 105.5°, presumably taken on a different region of the cantilever chip. Solvent-cleaned silicon samples and calcium fluoride films were used as hydrophilic substrates. As with the measurements of *Xiao* and *Qian*, contact angle measurements for the hydrophilic samples and tips were not presented. Results for hydrophobic and hydrophilic tips are shown in Fig. 32.10.

These results, which were carried out independently and without knowledge of *Xiao* and *Qian's* work, show impressive agreement. This is particularly interesting given that here the *tip* was varied from hydrophilic to hydrophobic (while the sample stayed hydrophilic), whereas in *Xiao* and *Qian's* work, the tip presumably remained hydrophilic and the sample was varied from hydrophilic to hydrophobic. For the hydrophobic tip, the pull-off force remains constant, indicating once again that capillary formation was suppressed. However, for the hydrophilic tip, three regimes of adhesion are found Fig. 32.11. Similar results are found for a hydrophilic glass microsphere used as a tip. The authors refer to these three regimes as the van der Waals regime, the mixed van der Waals–capillary regime, and the capillary regime. In agreement with *Xiao* and *Qian's* assessment, the authors propose that at low RH ($\lesssim$ 35% in this case), the formation of the water meniscus is suppressed and the adhesion is dominated by solid–solid (presumably van der Waals) interactions. They propose, based on the work of *de Gennes* on the theory of spreading [32.101], that a minimum precursor film thickness is required to form the meniscus. The authors also present a calculation of the adhesion force when assumptions (1) and (2) are relaxed.

32.4.3 Theoretical Issues Revisited

As detailed in Sect. 32.4.1, there are many approximations leading to (32.8). However, the geometrical assumptions (1)-(4), (7) and (8) are addressed by the numerical treatment of *Orr* et al. [32.106]. In this approach, the circle approximation is removed. Boundary conditions determined by the geometry are applied to the axisymmetric Young–Laplace differential equation,

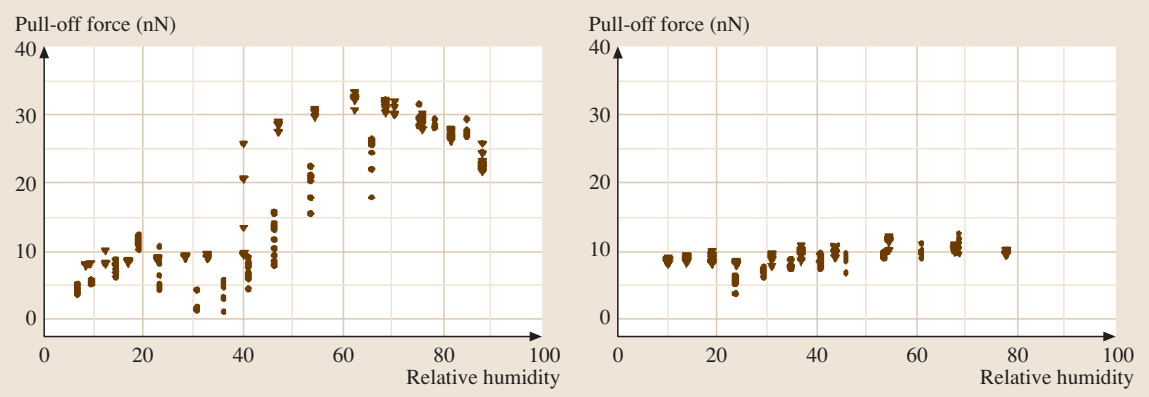

Fig. 32.10 **(a)** Pull-off force versus RH measured between a hydrophilic tip and a flat silicon sample. *Circles*: measured when increasing RH. *Triangles*: measured when decreasing RH. **(b)** Pull-off force versus RH measured between a sharp SFM tip coated with OTS and a flat silicon sample. The pull-off force is independent of humidity. After [32.118]

which is then solved exactly in terms of incomplete elliptic integrals. The total force is calculated from the Laplace pressure and the resolved surface tension force contributions, and is independent of the z-plane at which it is calculated. Let us qualitatively consider Fig. 32.12a, which is a revised form of Fig. 32.3 showing the "pendular bridge" geometry. Now we have replaced the commonly used radii r_1 and r_2 with the *principal radii of curvature*, r_a (the azimuthal radius) and r_m (the meridional radius). The principal radii are normal everywhere to the meniscus surface and are contained in two orthogonal planes. Each of these orthogonal planes contain the surface normal. Although any two orthogonal planes can be used to find the surface curvature, the principal radii are in the planes oriented such that they contain the minimum and maximum surface radii. Note that these quantities *are not constant – they have distinct local values at different locations on the meniscus surface*. The particular radii drawn refer to the point A on the meniscus surface. The radii drawn in Fig. 32.12a refer to, where the direction indicates the normal to the meniscus surface at A. Being outside the pendular ring, the meriodonal radius r_m is negative, and its magnitude is equal to the radius of curvature of the arc formed by the intersection of the plane of the page and the meniscus surface. Being inside the pendular ring, the azimuthal radius r_a is positive, and its magnitude is equal to the radius of curvature of the corresponding arc normal to the plane of the page.

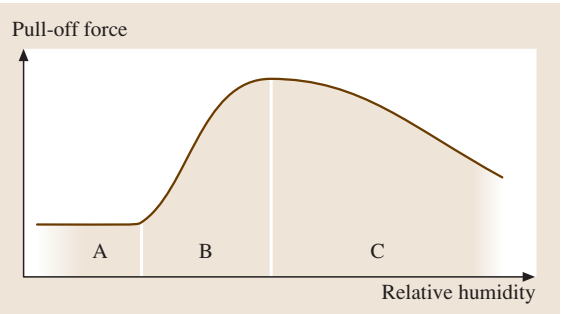

Fig. 32.11 Figure illustrating the distinct regimes of the pull-off force as a function of RH. Regimes I, II, and III are referred to as the van der Waals regime, mixed van der Waals–capillary regime, and capillary regime respectively. After [32.118]

Using r_a and r_m, the mensiscus is now isobaric. Equation (32.7) is no longer approximate, that is:

$$r_K^{-1} = \left(\frac{1}{r_m} + \frac{1}{r_a}\right) = \frac{RT}{\gamma V} \ln\left(\frac{p}{p_0}\right) . \qquad (32.11)$$

Let us take R to be small, say 20 nm, of the order of an AFM tip. At very low partial pressure p/p_0, the geometrical approximations leading to (32.8) hold, and (32.9) for the constant volume case and (32.10) for the constant Kelvin radius case still hold. However, for $D = 0$, as p/p_0 begins to increase, we see from Fig. 32.5 that $|r_K|$ begins to approach R. Recall that the azimuthal radius r_a is positive while the meridional radius r_m is negative. As p/p_0 increases, r_a begins to approach $|r_m|$ in magnitude because of the high tip curvature. Hence, $|r_m|$ must decrease to keep r_K (a negative quantity) constant. This significantly changes the meniscus profiles.

In Fig. 32.12b, we show our own calculated results following the numerical approach with $R = 20$ nm,

and assuming constant volume of the meniscus. As p/p_0 increases in Fig. 32.12b, with $D = 0$, we indeed see that the maximum height in the meridional profile becomes significantly smaller than r_K. More importantly, in Fig. 32.12c, we see the effect on the total force.

The inset in Fig. 32.12c shows the dependence of the maximum capillary force (at $D = 0$) versus p/p_0. We see that {eq08-d32-eq8 at $D = 0$ holds up well even at $p/p0 = 0.9$, where it is still 80% of the value predicted by the simple theory. This is because the resolved surface tension, when calculated at the circle of contact between the sphere and the asperity, begins to contribute significantly even though the area-dependent contribution from the Laplace pressure is reduced.

These exact numerical results substantiate the conclusions drawn earlier [32.44], that the strong decrease in pull-off force with increasing p/p_0 is not due to a decrease in the capillary adhesion. However, besides the tip shape argument already mentioned [32.44, 105], another explanation for the reduction in force at high RH has been proposed [32.104, 118]. From thermodynamics, the component of the attractive force acting on the

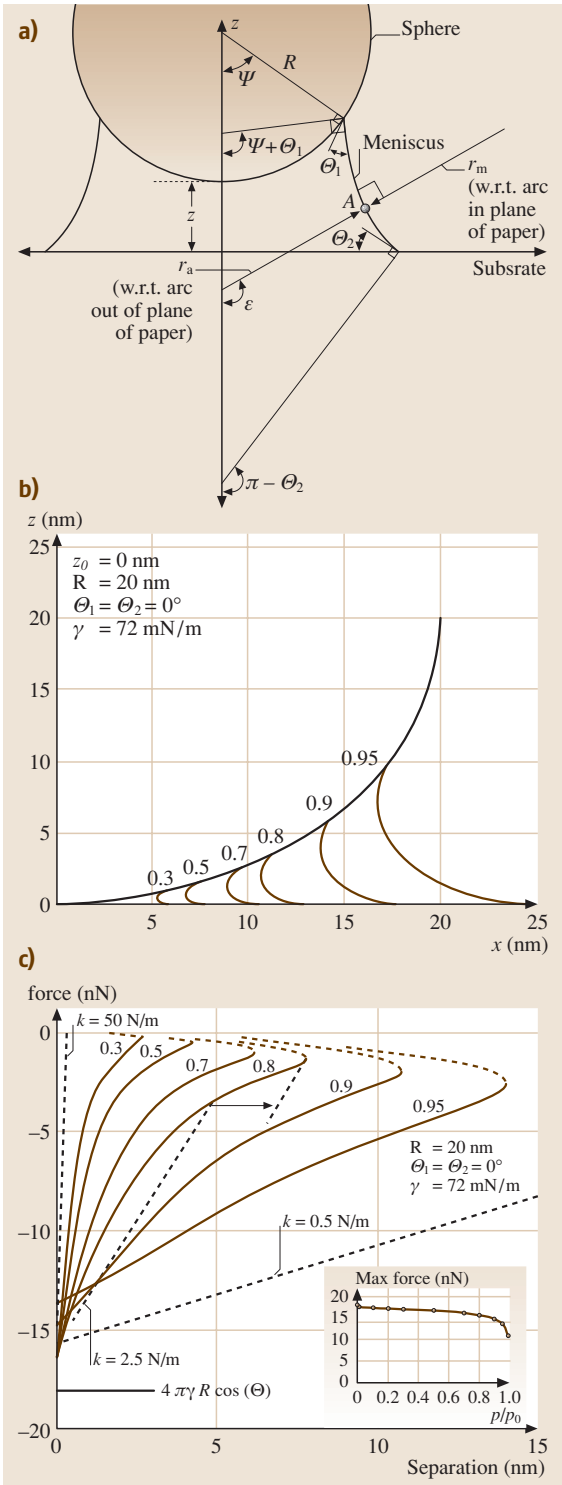

Fig. 32.12 **(a)** The general pendular ring geometry for a meniscus between a sphere of radius R and a flat substrate. The contact angles are θ_1 and θ_2 for the sphere and plane respectively. z represents the separation between the sphere and the flat surface. The local meridional radius of curvature, r_m (<0), and local azimuthal radius of curvature, r_a (>0), are drawn for the point A. **(b)** Geometric shape of a water meniscus for a range of RH values, from the numerical solution to the Young-Laplace equation for a 20 nm radius sphere at zero separation (contact) for perfectly hydrophilic surfaces. Clearly, the size of the meniscus starts to approach the size of the sphere itself at high RH. The lack of applicability of the circle approximation is also evident. **(c)** The meniscus force between the tip and the surface as a function of separation for a range of RH values from 0.3 to 0.95. The unstable part of the force–separation curve is indicated with a *dotted line*. *Dashed lines* represent the force–displacement relation for a cantilever with force constants of k =0.5, 2.5, and 50 N/m. Instabilities will occur when the gradient of the meniscus force exceeds k. A force constant of 50 N/m will remain stable for all RH, and one of 0.5 N/m will pull off immediately upon applying any retraction. At 2.5 N/m, metastable points may be reached depending on the RH. The *solid line* at the bottom represents the prediction of (32.8). The *inset* shows the maximum attractive force (at zero separation) as a function of RH

tip from the liquid in the gaps is given by

$$F_{\text{chem}} = -\frac{\partial G}{\partial z} = -\frac{A}{v} kT \ln\left(\frac{p}{p_0}\right) , \qquad (32.12)$$

where G is the Gibbs free energy, A is the area of the liquid film in the gap, and v is the molar volume. This term corresponds to a positive (repulsive) force opposing the negative (attractive) capillary force. For a small radius R, the relative importance of A increases, and hence this term can become important.

In addition, the force–displacement curves in Fig. 32.12c exhibit a "nose". Points below this nose (indicated by the solid lines) are stable capillary shapes, while points above it (indicated by the dotted lines) are unstable, and will not be accessed by an experiment. The dashed lines in Fig. 32.12c show the cantilever load lines for three different stiffnesses and are drawn for the case $p/p_0 = 0.8$. If the AFM cantilever is stiff, the full force–displacement curve, up to the tip of the nose, will be sampled. For example, *Binggeli* and *Mate* [32.104] used a spring stiffness of $\approx 50\,\text{N/m}$, and their results exhibit the full capillary force–displacement curves (they estimate $R = 100\,\text{nm}$). On the other hand, *Xiao* and *Qian* [32.105] used a nominal spring stiffness of $\approx 0.5\,\text{N/m}$. That stiffness would only measure the maximum force in this situation. The stiffnesses used by *He* et al. [32.118] were nominally 0.5 N/m and below. Indeed, they saw no dependence of the pull-off force on the spring constant. However, if the spring constant were 2.5 N/m with $p/p_0 = 0.8$, we would expect a jump from the maximum capillary force to another stable point. Beyond this point, the experiment would sample the remainder of the curve.

This pendular ring treatment has not considered that a thin film of liquid is present on the surface according to the BET adsorption isotherm [32.119], nor has it considered the associated effect of disjoining pressure. Disjoining pressure can be thought of as the force per unit area experienced by surface molecules on a solid surface relative to molecules on the bulk liquid [32.120]. Gao [32.121] has shown that the effect of disjoining pressure is small when $r_a \ll R$ and $D \ll D_{\max}$ (where $D_{\max}$ is the distance corresponding to rupture). Clearly these conditions are not always met by the pendular ring, and therefore experimental work to quantify the effect of disjoining pressure on the true capillary force-displacement curves of AFM-sized tips would be welcome.

There is a large body of literature exploring the numerical solution to the axisymmetric Young–Laplace differential equation. For example, *Lian* et al. [32.122] examined the stability of the curves in detail. *Willett* et al. [32.123] provide an excellent summary of this literature and of the macroscale experiments that have been conducted. They also perform experiments that match the theoretical curves using millimeter-sized spheres, and further give analytical expressions derived from curve fitting procedures to approximate the numerical results.

32.4.4 Future Directions

The results and modeling so far indicate the possibility of two trends: hydrophobic surfaces will exhibit little dependence of adhesion on RH, whereas if one surface is hydrophilic, three regimes of behavior occur: constant solid–solid adhesion at low RH, increasing adhesion at intermediate RH, and decreasing adhesion at the highest RH. Some insight into the physical mechanisms behind these regimes has been presented, but it would be desirable to pursue further work in this area.

Perhaps most critically needed is an atomic-scale picture of the menisci and water films present under low partial pressures. This could address the question of why adhesion is initially independent of RH, and when the meniscus itself would start to form. Further theoretical developments that address the assumptions laid out above would also help to clarify the picture. It is also important to extend these studies beyond simply the case of water, as the properties of other liquids are also of great interest, and could be compared to previous experiments with the SFA and other tools.

Studies that clarify the kinetics of meniscus formation are also needed. There should be a noticeable transition in behavior once the rate of displacement becomes comparable to the appropriate kinetic rates, and this could provide valuable information about these kinetic processes at the nanometer scale.

Finally, as mentioned before, there continues to be a gap in reproducibility and comparability between laboratories that will only be bridged when standard techniques for tip characterization and force and displacement calibration are addressed. Efforts that take these considerations into account are worthy of further support.

32.5 Self-Assembled Monolayers

32.5.1 Adhesion at SAM Interfaces

When thinking about adhesion and the related phenomenon of friction, it is important to realize that the interfaces of real surfaces in contact are rarely atomically smooth. Surfaces that appear smooth on the macroscopic scale are, upon closer inspection, found to consist of nanometer-scaled asperities (typically on the order of 10 nm) whose intentional or accidental interactions ultimately control adhesion, friction and wear at contacts [32.124–128]. The sizes of these asperities become particularly important when one considers that the true contact area between interfaces for the distribution of load is localized through these asperity–asperity interactions where extremely high pressures can be produced, resulting in sharply increasing local stress fields that can cause materials to yield and shear as they encounter each other during sliding and intermittent contact. In addition to load distribution at nanoscale asperity–asperity contacts, their size will influence surface wetting and adhesion due to capillary forces localized at the contacts [32.126–128]. The structures of applied lubricant films at such asperities will be highly dependent upon asperity curvature, and defects in lubricant film structure may form more readily here than on atomically flat surfaces.

The minimization of adhesion at such asperity–asperity contacts is a critical issue in MEMS devices [32.125–128]. In fact, the intentional introduction of surface roughness (on the order of 10 nm RMS) can be employed to lead to reduced stiction during post-processing feature release. These same asperities, however, must later resist wear during controlled or accidental contact during device operation. Thus, the specific details of adhesion and energy dissipation at such asperity–asperity contacts are required for the rational design of such systems.

To function as a protective lubricant layer in such systems, self-assembled monolayers (SAMs) of alkylsilane and fluorosilane compounds with chain lengths ranging from C_{10} to C_{18} have been shown to be useful in the reduction of friction and adhesion in MEMS [32.125–128]. Such direct applications of SAMs as lubricant films, combined with the ease of sample preparation and the ability to generate model surfaces with well defined film chemistry and structures have made nanotribological and adhesion studies of SAMs a rich area of research [32.5]. Many of these nanotribological studies have used AFM to examine either SAMs of alkylsilane films on atomically smooth Si wafers, glass or mica surfaces. Alternatively, many researchers have examined alkanethiol films on atomically smooth Au(111) surfaces. Using this approach many molecular level details, such as the influence of film chemistry and molecular organization on friction, adhesion and wear of SAMs can be obtained. Developing a clear understanding of the details of adhesion at SAM-modified surfaces allows for the complex link between surface chemistry and adhesion and friction to be understood at the molecular level. In this section we overview AFM studies of adhesion on SAM-modified surfaces.

32.5.2 Chemical Force Microscopy: General Methodology

In order to probe adhesion between chemical modified surfaces using AFM, the probe tips and sample surfaces are typically modified via self-assembly of monolayers using organosilanes on surfaces such as mica, glass or oxidized Si or Si_3N_4 (the latter two being the typical materials of which AFM tips are made) or formed from thiols on Au-coated AFM tips and surfaces (Fig. 32.12) [32.129, 130]. While this has been shown to be a facile method for the modification of AFM tips for chemical force measurements, it should be noted that the details of the packing densities of the monolayers formed on the AFM tips are in general not known. This lack of detail regarding molecular overlayers on AFM probe tips can be a problem which requires careful consideration when using such chemically modified tips for the quantitative determination of adhesion forces and molecular interactions, as the number density of species in the tip–sample contact is related to the measured adhesion.

Details of the environment in which the adhesion measurements are carried out are another important consideration. Under ambient environmental lab conditions, surfaces are contaminated with organic compounds from the air as well as a layer of condensed water vapor, which varies with humidity. The condensed water layer can form a contact meniscus between the tip and sample introducing a capillary force into the measured adhesion [32.131]. The presence of this capillary force can overwhelm the details of the adhesion from the SAM-terminated surfaces to be probed. To avoid this, many studies are performed in liquid environments or ultra-high vacuum to eliminate capillary forces. In liquid, the nature of the solvent will of course impact on the meas-

ured adhesion for a given pair of interacting surfaces, as solvent exclusion plays an important role. Also, in the case of water, the pH and ionic strength of the water environment can also influence the measured adhesion in the presence of any surface-bound charges.

When quantifying adhesion energies from AFM measurements, the contact mechanics model developed by *Johnson*, *Kendall* and *Roberts* (JKR) [32.22, 111] is often employed in the analysis of the adhesion data acquired by force–distance spectroscopy, whereby the number of interacting species (and consequently the average 'unit' interaction force or energy) can be derived from the estimated contact area and the average molecular packing density. Using the JKR model, the force of adhesion (AFM pull-off force) is related to the work of adhesion, W_{adh}, and the reduced radius, R, of the tip–surface contact:

$$F_{\mathrm{adh}} = -\frac{3}{2}\pi R W_{\mathrm{adh}} \,. \tag{32.13}$$

The work of adhesion is a combination of the tip–surface (γ_{ts}), tip–solvent (γ_{tl}) and surface–solvent (γ_{sl}) interfacial energies ($W_{\mathrm{adh}} = \gamma_{\mathrm{sl}} + \gamma_{\mathrm{tl}} - \gamma_{\mathrm{ts}}$), and for tip–surface combinations that have the same chemical composition, the surface energy may be estimated directly from the adhesion measurement as W_{adh}. The effective contact radius at separation, r_{s}, from the JKR model is given as:

$$r_{\mathrm{S}} = \left(\frac{3\pi W_{\mathrm{adh}} R^2}{2K}\right)^{\frac{1}{3}} \,, \tag{32.14}$$

where K is the reduced elastic modulus of the tip and surface. Using the contact area at separation and the assumed packing density of the molecules at the surfaces in contact, an estimate of the adhesion force or interaction energy can be made on a per molecule basis.

The accuracy of the interfacial energies and per molecule values obtained using this approach, however, must be considered carefully due to the accumulation of error carried though by the imprecise knowledge of the contact, including the tip radius, molecular packing densities of the modified surfaces, as well as the associated elastic properties of the contact at the monolayer level. As the details of the elastic properties of self-assembled monolayers are generally not known, the elastic properties of the contacts are typically assumed to be dominated by those of the underlying substrate, and the bulk values of the surface and/or tip materials (Au, Si, mica, Si_3N_4, SiO_2) are often employed in these calculations. Moreover, as mentioned above, if the molecular packing densities of the monolayers being evaluated are not known (as is the case with a typical AFM tip), then estimations must be used. For contact areas at pull-off approaching 1 nm^2, if the error in packing density is as much as one molecule per nm^2, for a typical alkanethiol this can lead to an error as high as 25% or more in the reported per molecule adhesion force, and such details should be taken into consideration when describing quantitative measurements.

An alternative approach to the measurement of adhesive interactions based on Poisson statistics has been promoted by *Beebe* and coworkers for the statistical evaluation of single bond forces without a priori knowledge of tip–surface contact details involved [32.132–134]. A main limitation of this approach, however, is that a completely homogeneous chemical system is assumed, so that there is only one type of discrete interaction present that gives rise to the observed adhesion. Unfortunately, for many solution phase systems a number of different interactions are typically operating, including energetic exchange with and reorganization of solvent molecules, depending on the solution conditions, issues that have never been thoroughly addressed in any molecular level measurement of adhesion.

32.5.3 Adhesion at SAM-Modified Surfaces in Liquids

A number of researchers have used AFM to probe interfacial adhesion for a variety of different chemical systems. Most notably, *Lieber* and coworkers promoted the use of chemically modified substrates and AFM tips to study selective molecular interactions [32.129, 135–139]. A number of other researchers have adopted a similar methodology leading to the measurement of adhesion forces and interfacial energies for the interactions of a variety of molecular functional groups in various environments, although to date few specific types of interactions have been thoroughly investigated (Table 32.1) [32.36, 129, 132, 135, 136, 140–149].

Measurements in air suffer from issues due to water vapor, as described above, so the adhesion of many SAM-terminated surfaces have been evaluated under liquid and it is these systems that we shall focus on here. The value of the adhesion is of course modified depending on the solvent. For example, the interaction of methyl-terminated interfaces is much stronger in water than in nonpolar solvents, in agreement with the general concept that upon separation the generation of hydrophobic interfaces in a polar solvent is highly energetically unfavorable. The impact of solvent on adhesion

can be addressed basically as a variation in the Hamaker constant.

When ionizable end-groups are studied in water, the details of the adhesion measurements and results become more complicated, as the chemical natures of the surfaces are now dependent on the pH and ionic strength of the solution. In these circumstances, multiple interactions including ionic, van der Waals and double-layer forces come into play simultaneously. Under these conditions, the general form for the JKR adhesion force may be modified to include these additional forces as follows:

$$F_{\mathrm{adh}} = -\frac{3}{2}\pi R W_{\mathrm{adh}} - \frac{AR}{6D} + 6\pi R W_{\mathrm{dl}} \,, \qquad (32.15)$$

where the second term now includes the attractive van der Waals component and the third term is the repulsive double-layer.

Table 32.1 List of various interactions evaluated by atomic force microscopy adhesion measurements

Chemical Contacts	References
$-CH_3/-CH_3$	[32.133, 135–137, 143] [32.146–148, 150]
$-CH_3/-COOH$	[32.135, 136, 150]
$-CH_3/-CONH_2$	[32.150]
$-CH_3/-NH_2$	[32.150]
$-CH_3/-OH$	[32.150]
$-CF_3/-CF_3$	[32.147]
$-CF_3/-CH_3$	[32.147]
$-OH/-OH$	[32.36, 133, 134, 137] [32.141, 148, 150]
$-OH/NH_2$	[32.150]
$-OH/-COOH$	[32.137, 150]
$-OH/-CONH_2$	[32.150]
$-COOH/-COOH$	[32.36, 132, 136, 137] [32.143, 148, 150]
$-CONH_2/-CONH_2$	[32.150]
$-CONH_2/-COOH$	[32.150]
$-NH_2/-NH_2$	[32.137, 150, 151]
$-CH_3/-NH_2$	[32.150, 151]
$-NH_2/-COOH$	[32.150]
$-NH_2/-CONH_2$	[32.150]
$-SO_3H/-SO_3H$	[32.151]
$-CH_3/-SO_3H$	[32.151]
$-NH_2/-SO_3H$	[32.151]
$-PO_3H_2/-PO_3H_2$	[32.152, 153]
$-SH/-SH$	[32.134]
$Au-Au$	[32.154]

Several groups have utilized the ability of AFM to function as a local probe of ionicity and to carry out local force titration measurements on several functional groups including $-COOH$ [32.36, 132, 136, 137, 143, 148, 150], $-NH_2$ [32.137, 150, 151], $-SO_3H$ [32.151] and $-PO_3H_2$ [32.152, 153] Table 32.1. The force–distance curves themselves can give a general sense of the local chemical state based on whether the approach curve is attractive or repulsive. In force titrations, the adhesion is measured as a function of pH, and the change in force is dependent upon the equilibrium mixture of charged species within the tip–sample contact at the time of measurement. Peaks in the adhesion force versus pH permit the determination of the local pK values for the ionized species, which are shown to be dependent on ionic strength. Shown in Fig. 32.13 is a force titration of a diprotic acid (11-thioundecyl-1-phosphonic acid). Shifts in the pK values from those measured in free solution have been ascribed to a variety of factors including build-up of excess surface charge and solvation effects of the surface-bound ionic species. However, the localization of charge and change migration are effects that are yet to be fully explored in these systems.

32.5.4 Impact of Intra- and Interchain Interactions on Adhesion

Several studies of the effect of chain length on friction and adhesion have found that in general, adhesion decreases with increasing chain length due to increased stability from lateral chain–chain van der Waals interactions within the film, which increases the overall film stiffness. The increased stiffness of the films acts to reduce the effective contact area that develops under compression, consequently reducing adhesion and friction [32.142, 144, 155]. However, in alkyl chain-based monolayers, the end-group orientation is also dependent on chain length. This results in an "odd–even" effect on the measured adhesion/friction of the monolayer. With $-CH_3$ terminated films, the methyl group orientation differs for odd- and even-length molecules. This impacts the orientation of the methyl group net dipole and hence the local surface free energy [32.156]. In circumstances where interchain hydrogen bonding can occur, additional film stability can be introduced, also yielding an "odd–even" effect, as observed by *Houston* and coworkers [32.140, 143].

AFM studies of alkanethiol films on Au surfaces have shown that, depending upon the tip size, under varying loads, the tip can readily penetrate the SAM film, displacing the thiol layer from the tip–sample con-

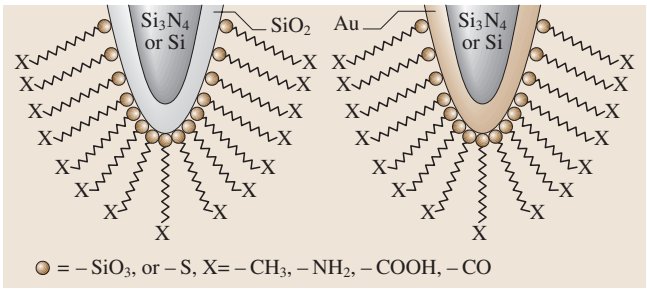

Fig. 32.13 The modification of AFM tips for chemical force microscopy is frequently carried out via chemical functionalization by alkylsilane monolayers on the oxidized surfaces of Si- or Si_3N_4-based tips or with alkylthiol monolayers assembled on Au-coated (≈ 50 nm) AFM tips. The Au tips often also have a Cr binding layer (≈ 5 nm) placed on before Au coating

tact [32.157–159]. Upon reduction of the force, the tip again moves out of the SAM film and the surface structure is returned to its original condition. Of key importance in such studies is the mechanism by which the film is displaced. Recently, this has been modeled using molecular dynamics simulations by *Harrison* [32.160]. These studies have clearly demonstrated that in the initial stages of film compression and penetration by an asperity, *gauche* defects within the typically all-*trans* configurations of molecules in the SAM layers appear and propagate. The introduction of such defects is the catalyst for the weakening of the chain–chain lateral interactions that help stabilize and maintain film integrity. As this is lost, the asperity can rapidly penetrate the film and alkanethiol displacement can occur either via chain collapse or bond scission from the surface. *Salmeron* and coworkers demonstrated that the prevalence of molecular displacement versus film compression depends heavily on the AFM tip size, with sharp tips readily penetrating and displacing surface-bound thiols, while large tips spread the load over more molecules and induce compression over displacement (Fig. 32.14).

The inherent stability of the film structure has also been confirmed by sum-frequency generation spectroscopic studies which have indicated that without the presence of lateral chain–chain interactions, *gauche* defects appear within the chain structure that reduce overall order and lateral interactions within films [32.73, 161]. The ability to form these defects through poor film order will consequently increase adhesion, friction and wear of the film. This same spectroscopic study further demonstrated that the appearance of *gauche* defects can be induced by controlling the local environment (with the presence of water), causing chains to collapse back upon themselves.

As the molecular structure in SAMs moves away from ideally organized layers, chain–chain interactions between the contacting surfaces can also result in entanglements. A recent study of the adhesive interactions of Au(111) surfaces modified with dialkylsulfides $[CH_3(CH_2)_n - S - (CH_2)_9CH_3;\ n = 9, 11, 13, 15, 17]$ with varying chain arm lengths probed the combined effect of chain length, solvent and intersurface chain entanglement on friction and adhesion using simultaneously modified surfaces and AFM tips [32.162]. This study found that chain–chain interpenetration produced the reverse dependence on chain length for the meas-

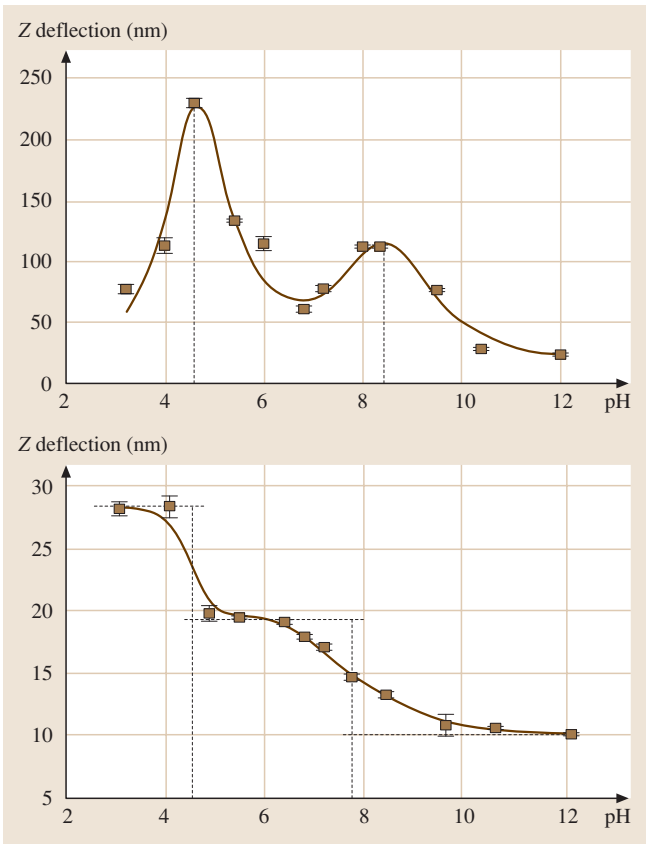

Fig. 32.14a,b Adhesion versus pH for 11-thioundecyl-1-phosphonic acid in buffer illustrating the impact of pH and ionic strength, **(a)** 10^{-4}M and **(b)** 10^{-1} M, on the measured adhesion. The peaks in adhesion provide local measures of the surface pK. After [32.153]

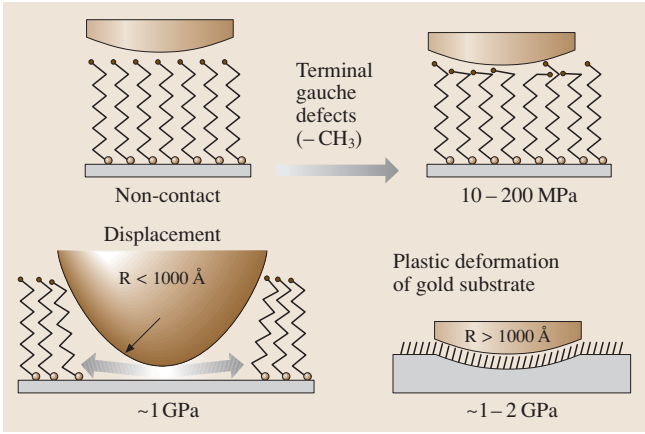

Fig. 32.15 Schematic illustrating the compression of a model lubricant layer under an AMF tip. At low pressures, *gauche* defects can form at the tip–sample junction but the molecules remain in place. Depending on the tip size and load, displacement (for sharp tips) or trapping of monolayer molecules (for blunt tips) can occur. After [32.5]

ured adhesion mentioned above. This work points to the need to examine the nature of intersurface chain entanglements in nanoscale systems. Such entanglements should be more prevalent in asperity–asperity contacts where ideal film structure will not be feasible.

32.5.5 Adhesion at the Single-Bond Level

The ability to resolve the discrete components of interactions is highly desirable. There have been few reports of the direct observation of discrete force components observed with the separation of an AFM tip from a surface. *Beebe* and coworkers have utilized a statistical method (as described above) for the direct determination of single-bond forces for a variety of interactions [32.132–134], including biological systems such as biotin–avidin [32.163, 164]. The first report of quantized force measurements was described by *Hoh* et al., which lead to the estimation of single hydrogen bonding forces from studies of glass surfaces in water as being on the order of 10 pN [32.165]. The use of AFM for the study of the energetics of true single chemical bond cleavage has also received little attention. One previous report described discrete covalent bond scission using AFM. In that case it was proposed that the jumps in the observed pull-off curves were due to sequential scission of chemical bonds contained in a large multifunctional polymeric species as it progressively detached from the substrate [32.166]. However, the identification of the relevant chemical bonds involved at each stage was largely based on the known (gas phase) bond strengths of the potentially active functional groups, such that solvation effects on the bond energies were ignored – a simplification that profoundly affects the estimated energetics, as energetic exchange with the solvent must be included. More recently, the measurement of discrete bond scission was reported by *Frisbie* and coworkers for Au-thiol complexes. Here the details of Au atom abstraction were reported with a quantized value of 100 pN (estimated at $\approx$ 10 kJ/mol, based on an assumed bond rupture length of 1 Å) [32.149]. These studies have demonstrated the feasibility of probing local single-bond energetics, and have suggested some general requirements for the measurement of adhesion quantization in SAM layers, including the need for a significant negative tip–surface interfacial energy coupled with minimal

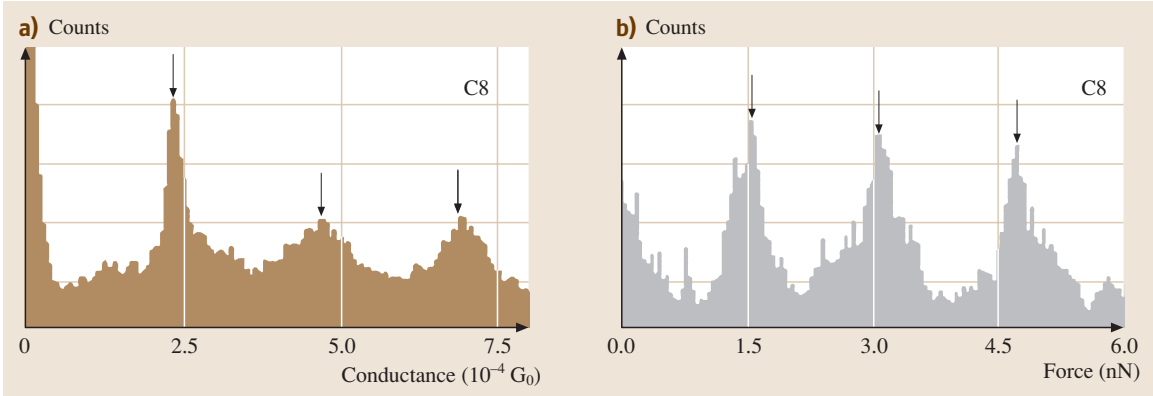

Fig. 32.16 Conductance and adhesion force distributions for 1,8′-octanedithiol, illustrating the quantization of the both the conductance and associated forces within the junction. After [32.154]

solvent surface tension [32.149,167]. More recently, discrete bond forces and the associated quantized changes in through-molecule conductance have been reported by *Tao* and coworkers (Fig. 32.16) [32.154]. These measurements have shown how the electrical and mechanical properties of bonds are linked within molecules. Here quantized values for Au–Au bond scission were reported to be on the order of ≈ 1.5 nN for 1,8′-octanedithiol. These measurements offer the ability to quantify not only molecular forces and bonds at the single molecule level, but also to determine how charge transport within molecules is impacted by the mechanical deformation of the molecules within the junction, a key element in developing measurements of single-molecule conduction critical to molecular-based electronic devices.

32.5.6 Future Directions

Extending AFM adhesion measurements to reactive systems where chemical bonds can form between the tip and surface affords an expansion of chemical reaction dynamics to solution-based chemistries, whereby the energetic details of single reaction events previously only accessible for gas phase scattering experiments may be obtained. Studies of such complex heterogeneous systems will open the door to evaluations of the energetic pathways of solution-based chemistries for any system where the appropriate functionalization of surfaces can be exploited. Adhesion has already been demonstrated as a reasonable local probe of surface reaction kinetics whereby the local changes in the chemical forces may be followed as a function of time during surface chemical reactions [32.168, 169]. In addition to advances in measurements of reactive systems by AFM, complete insight into the operative molecular mechanisms can only be gained when combined with a detailed theory that takes into account not only the specific types of interactions present between the surfaces, but also the requisite energetic exchange with local solvent molecules. Advances in computer technologies and in computational theory have made this realistic [32.145].

To advance the field of adhesion measurements at the molecular level, energetic barriers for specific interactions also need to be evaluated, with attention given to the nature of the molecular interactions being probed, importantly including the details of energetic exchange with the solvent surrounding the interacting molecules. Studies by AFM of molecular interactions within sharply confined geometries ($\approx 1\,\mathrm{nm}^2$ contact area) provide an opportunity to evaluate such contributions with molecular detail. Here again, *Lieber* and coworkers have been advancing the approach of chemically functionalizing carbon nanotubes to reduce both the type and number of specific interacting species [32.138]. This approach may hold some promise for probing well-defined specific chemical interactions and/or reactions as long as the nanotubes can be sufficiently stabilized against the buckling that is predicted by recent theoretical studies [32.160].

In addition to the modification of probe geometries to improve the localization of interactions for adhesion measurements, one of the principal difficulties with performing AFM measurements of adhesion at SAM surfaces is the unavoidable snap to contact. This makes details about the long-range interaction potential almost completely inaccessible. To address this issue, *Lieber* and coworkers have developed a modified AFM system in which the cantilever is magnetized, providing an additional feedback mechanism to help avoid snap-in [32.36]. When used, this approach provides a smooth approach and retract curve. Similarly, the capacitive coupling feedback mechanism of the interfacial force microscope (IFM) also affords measurements of this transition from out of contact without snap-in [32.140].

32.6 Concluding Remarks

Scanning probes are powerful tools for determining the fundamental molecular basis of adhesion. Continuum models of adhesion and capillary condensations are useful, but careful attention must be paid to their limits and assumptions. Further progress in these areas requires detailed analysis of the structure and chemistry of both the tip and sample, as well as their environment (solvent, humidity, and so on).

The ability to determine the effects of molecular-scale water menisci or single-bond energetics are truly spectacular accomplishments that continue to inspire researchers worldwide to pursue these measurements. With attention paid to previous work and a consideration of the issues raised in this chapter, many more discoveries are sure to be made.

References

32.1 J. N. Israelachvili: *Intermolecular and Surface Forces* (Academic Press, London 1992)

32.2 K. Autumn, Y. A. Liang, S. T. Hsieh, W. Zesch, C. Wai Pang, T. W. Kenny, R. Fearing, R. J. Full: Adhesive force of a single gecko foot-hair, Nature **405**, 681–685 (2000)

32.3 A. L. Baldwin, G. Thurston: Mechanics of endothelial cell architecture and vascular permeability, Crit. Rev. Biomed. Eng. **29**, 247–278 (2001)

32.4 S. R. White, N. R. Sottos, P. H. Guebelle, J. S. Moore, M. R. Kessler, S. R. Sriram, E. N. Brown, S. Viswanathan: Autonomic healing of polymer composites, Nature **409**, 794–797 (2001)

32.5 R. W. Carpick, M. Salmeron: Scratching the surface: Fundamental investigations of tribology with atomic force microscopy, Chem. Rev. **97**, 1163–1194 (1997)

32.6 M. P. De boer, T. A. Michalske: Accurate method for determining adhesion of cantilever beams, J. Appl. Phys. **86**, 817–827 (1999)

32.7 M. P. De boer, J. A. Knapp, T. A. Michalske, U. Srinivasan, R. Maboudian: Adhesion hysteresis of silane-coated microcantilevers, Acta Mater. **48**, 4531–4541 (2000)

32.8 R. Maboudian, R. T. Howe: Critical review: Adhesion in surface micromechanical structures, J. Vacuum Sci. Technol. **15**, 1–20 (1997)

32.9 R. Maboudian, W. R. Ashurst, C. Carraro: Tribological challenges in micromechanical systems, Tribol. Lett. **12**, 95–100 (2002)

32.10 R. Maboudian: Adhesion and friction issues associated with reliable operation of MEMS, MRS Bull. **23**, 47–51 (1998)

32.11 J. N. Israelachvili: Thin film studies using multiple-beam interferometry, J. Colloid Interf. Sci. **44**, 259–272 (1973)

32.12 J. N. Israelachvili, D. Tabor: The measurement of van der Waals dispersion forces in the range of 1.5 to 130 nm, Proc. R. Soc. Lond. A **331**, 19–38 (1972)

32.13 G. Binnig, C. F. Quate, C. Gerber: Atomic force microscope, Phys. Rev. Lett. **56**, 930–933 (1986)

32.14 J. N. Israelachvili, P. M. Mcguiggan, A. M. Homola: Dynamic properties of molecularly thin liquid films, Science **240**, 189–191 (1988)

32.15 J. Peachey, J. Van Alsten, S. Granick: Design of an apparatus to measure the shear response of ultrathin liquid, Rev. Sci. Instrum. **62**, 463–473 (1991)

32.16 P. Frantz, N. Agraït, M. Salmeron: Use of capacitance to measure surface forces. 1. Measuring distance of separation with enhanced spatial and time resolution, Langmuir **12**, 3289–3294 (1996)

32.17 L. R. Fisher, J. N. Israelachvili: Direct measurement of the effect of meniscus forces on adhesion: a study of the applicability of macroscopic thermodynamics to microscopic liquid interfaces, Colloids and Surfaces **3**, 303–319 (1981)

32.18 L. R. Fisher, J. N. Israelachvili: Experimental studies on the applicability of the Kelvin equation to highly curved concave menisci, J. Colloid Interf. Sci. **80**, 528–541 (1981)

32.19 J. N. Israelachvili: Adhesion, friction and lubrication of molecularly smooth surfaces. In: *Fundamentals of Friction*, ed. by I. L. Singer, H. M. Pollock (Kluwer, Dordrecht 1992) pp. 351–385

32.20 G. Reiter, A. L. Demirel, J. Peanasky, L. L. Cai, S. Granick: Stick to slip transition and adhesion of lubricated surfaces in moving contact, J. Chem. Phys. **101**, 2606–2615 (1994)

32.21 S. Granick: Molecular tribology of fluids. In: *Fundamentals of Friction*, ed. by I. L. Singer, H. M. Pollock (Kluwer, Dordrecht 1992) p. 387

32.22 K. L. Johnson: *Contact Mechanics* (University Press, Cambridge 1987)

32.23 M. A. Lantz, S. J. O'shea, M. E. Welland: Simultaneous force and conduction measurements in atomic force microscopy, Phys. Rev. B **56**, 15345–15352 (1997)

32.24 M. Enachescu, R. J. A. Van Den Oetelaar, R. W. Carpick, D. F. Ogletree, C. F. J. Flipse, M. Salmeron: An AFM study of an ideally hard contact: The diamond(111)/tungsten-carbide interface, Phys. Rev. Lett. **81**, 1877–1880 (1998)

32.25 M. A. Lantz, S. J. O'shea, A. C. F. Hoole, M. E. Welland: Lateral stiffness of the tip and tip–sample contact in frictional force microscopy, Appl. Phys. Lett. **70**, 970–972 (1997)

32.26 R. W. Carpick, D. F. Ogletree, M. Salmeron: Lateral stiffness: A new nanomechanical measurement with friction force microscopy, Appl. Phys. Lett. **70**, 1548–1550 (1997)

32.27 O. Marti, B. Drake, P. K. Hansma: Atomic force microscopy of liquid-covered surfaces: atomic resolution images, Appl. Phys. Lett. **51**, 484–486 (1987)

32.28 G. J. Germann, S. R. Cohen, G. Neubauer, G. M. Mcclelland, H. Seki, D. Coulman: Atomic scale friction of a diamond tip on diamond (100) and (111) surfaces, J. Appl. Phys. **73**, 163–167 (1993)

32.29 L. Howald, E. Meyer, R. Lüthi, H. Haefke, R. Overney, H. Rudin, H.-J. Güntherodt: Multifunctional probe microscope for facile operation in ultrahigh vacuum, Appl. Phys. Lett. **63**, 117–119 (1993)

32.30 M. Kageshima, H. Yamada, K. Nakayama, H. Sakama, A. Kawau, T. Fujii, M. Suzuki: Development of an ultrahigh vacuum atomic force microscope for investigations of semiconductor surfaces, J. Vacuum Sci. Technol. B **11**, 1987–1991 (1993)

32.31 J. A. Greenwood: Adhesion of elastic spheres, Proc. R. Soc. Lond. A **453**, 1277–1297 (1997)

32.32 S. P. Jarvis, A. Oral, T. P. Weihs, J. B. Pethica: A novel force microscope and point contact probe, Rev. Sci. Instrum. **64**, 3515–3520 (1993)

32.33 S. P. Jarvis, H. Yamada, S.-I. Yamamoto, H. Tokumoto: A new force controlled atomic force microscope for use in ultrahigh vacuum, Rev. Sci. Instrum. **67**, 2281–2285 (1996)

32.34 S. A. Joyce, J. E. Houston: A new force sensor incorporating force-feedback control for interfacial force microscopy, Rev. Sci. Instrum. **62**, 710–715 (1991)

32.35 S. A. Joyce, J. E. Houston, T. A. Michalske: Differentiation of topographical and chemical structures using an interfacial force microscope, Appl. Phys. Lett. **60**, 1175 (1992)

32.36 P. D. Ashby, L. W. Chen, C. M. Lieber: Probing intermolecular forces and potentials with magnetic feedback chemical force microscopy, J. Am. Chem. Soc. **122**, 9467–9472 (2000)

32.37 H. I. Kim, V. Boiadjiev, J. E. Houston, X. Y. Zhu, J. D. Kiely: Tribological properties of self-assembled monolayers on Au, SiO_x, Si surfaces, Tribol. Lett. **10**, 97–101 (2001)

32.38 P. A. Taylor, J. S. Nelson, B. W. Dodson: Adhesion between atomically flat metallic surfaces, Phys. Rev. B **44**, 5834–5841 (1991)

32.39 J. S. Nelson, B. W. Dodson, P. A. Taylor: Adhesive avalanche in covalently bonded materials, Phys. Rev. B **45**, 4439–4444 (1992)

32.40 R. Garcia, R. Perez: Dynamic atomic force microscopy methods, Surf. Sci. Rep. **47**, 197–301 (2002)

32.41 F. J. Giessibl: Forces and frequency shifts in atomic-resolution dynamic-force microscopy, Phys. Rev. B **56**, 16010–15 (1997)

32.42 P. M. Hoffmann, A. Oral, R. A. Grimble, H. O. Ozer, S. Jeffery, J. B. Pethica: Direct measurement of interatomic force gradients using an ultra-low-amplitude atomic force microscope, Proc. R. Soc. Lond. A **457**, 1161–1174 (2001)

32.43 K. R. Shull: Contact mechanics and the adhesion of soft solids, Mater. Sci. Eng. R **R36**, 1–45 (2002)

32.44 L. Xu, A. Lio, J. Hu, D. F. Ogletree, M. Salmeron: Wetting and capillary phenomena of water on mica, J. Phys. Chem. B **102**, 540–548 (1998)

32.45 S. P. Timoshenko, J. N. Goodier: *Theory of Elasticity* (McGraw-Hill, New York 1987)

32.46 J. P. Cleveland, S. Manne, D. Bocek, P. K. Hansma: A nondestructive method for determining the spring constant of cantilevers for scanning force microscopy, Rev. Sci. Instrum. **64**, 403–405 (1993)

32.47 J. E. Sader, I. Larson, P. Mulvaney, L. R. White: Method for the calibration of atomic force microscope cantilevers, Rev. Sci. Instrum. **66**, 3789–3798 (1995)

32.48 M. Tortonese, M. Kirk: Characterization of application specific probes for SPMs, Proc. SPIE **3009**, 53–60 (1997)

32.49 T. R. Albrecht, S. Akamine, T. E. Carver, C. F. Quate: Microfabrication of cantilever styli for the atomic force microscope, J. Vacuum Sci. Technol. A **8**, 3386–96 (1990)

32.50 H.-J. Butt, P. Siedle, K. Seifert, K. Fendler, T. Seeger, E. Bamberg, A. L. Weisenhorn, K. Goldie, A. Engel: Scan speed limit in atomic force microscopy, J. Microsc. **169**, 75–84 (1993)

32.51 J. M. Neumeister, W. A. Ducker: Lateral, normal, and longitudinal spring constants of atomic force microscopy cantilevers, Rev. Sci. Instrum. **65**, 2527–2531 (1994)

32.52 J. E. Sader: Parallel beam approximation for V-shaped atomic force microscope cantilevers, Rev. Sci. Instrum. **66**, 4583–4587 (1995)

32.53 D. F. Ogletree, R. W. Carpick, M. Salmeron: Calibration of frictional forces in atomic force microscopy, Rev. Sci. Instrum. **67**, 3298–3306 (1996)

32.54 R. Lüthi, E. Meyer, H. Haefke, L. Howald, W. Gutmannsbauer, M. Guggisberg, M. Bammerlin, H.-J. Güntherodt: Nanotribology: An UHV-SFM study on thin films of C_{60} and AgBr, Surf. Sci. **338**, 247–260 (1995)

32.55 U. D. Schwarz, P. Koster, R. Wiesendanger: Quantitative analysis of lateral force microscopy experiments, Rev. Sci. Instrum. **67**, 2560–2567 (1996)

32.56 T. J. Senden, W. A. Ducker: Experimental determination of spring constants in atomic force microscopy, Langmuir **10**, 1003–1004 (1994)

32.57 A. Torii, M. Sasaki, K. Hane, S. Okuma: A method for determining the spring constant of cantilevers for atomic force microscopy, Meas. Sci. Technol. **7**, 179–184 (1996)

32.58 J. A. Ruan, B. Bhushan: Atomic-scale friction measurements using friction force microscopy: Part I – general principles and new measurement techniques, Trans. ASME J. Tribol. **116**, 378–388 (1994)

32.59 Y. Q. Li, N. J. Tao, J. Pan, A. A. Garcia, S. M. Lindsay: Direct measurement of interaction forces between colloidal particles using the scanning force microscope, Langmuir **9**, 637–641 (1993)

32.60 J. E. Sader, J. W. M. Chon, P. Mulvaney: Calibration of rectangular atomic force microscope cantilevers, Rev. Sci. Instrum. **70**, 3967–3969 (1999)

32.61 J. S. Villarrubia: Morphological estimation of tip geometry for scanned probe microscopy, Surf. Sci. **321**, 287–300 (1994)

32.62 J. S. Villarrubia: Algorithms for scanned probe microscope image simulation, surface reconstruction, and tip estimation, J. Res. Natl. Inst. Stand. Technol. (USA) **102**, 425–454 (1997)

32.63 L. S. Dongmo, J. S. Villarrubia, S. N. Jones, T. B. Renegar, M. T. Postek, J. F. Song: Experimental test of blind tip reconstruction for scanning probe microscopy, Ultramicroscopy **85**, 141–153 (2000)

32.64 R. W. Carpick, N. Agraït, D. F. Ogletree, M. Salmeron: Measurement of interfacial shear (friction) with an ultrahigh vacuum atomic force microscope, J. Vacuum Sci. Technol. B **14**, 1289–1295 (1996)

32.65 K. F. Jarausch, T. J. Stark, P. E. Russell: Silicon structures for in situ characterization of atomic force microscope probe geometry, J. Vacuum Sci. Technol. B **14**, 3425–3430 (1996)

32.66 F. Atamny, A. Baiker: Direct imaging of the tip shape by AFM, Surf. Sci. **323**, L314–L318 (1995)

32.67 S. S. Sheiko, M. Moller, E. M. C. M. Reuvekamp, H. W. Zandbergen: Evaluation of the probing profile of scanning force microscopy tips, Ultramicroscopy **53**, 371–380 (1994)

32.68 C. Odin, J. P. Aimé, Z. El Kaakour, T. Bouhacina: Tip's finite size effects on atomic force microscopy in the contact mode: Simple geometrical considerations for rapid estimation of apex radius, tip angle based on the study of polystyrene latex balls, Surf. Sci. **317**, 321–340 (1994)

32.69 K. L. Westra, D. J. Thomson: Atomic force microscope tip radius needed for accurate imaging of thin film surfaces, J. Vacuum Sci. Technol. B **12**, 3176–3181 (1994)

32.70 P. Markiewicz, M. C. Goh: Atomic force microscope tip deconvolution using calibration arrays, Rev. Sci. Instrum. **66**, 3186–3190 (1995)

32.71 R. Dixson, J. Schneir, T. Mcwaid, N. Sullivan, V. W. Tsai, S. H. Zaidi, S. R. J. Brueck: Toward accurate linewidth metrology using atomic force microscopy and tip characterization, Proc. SPIE **2725**, 589–607 (1996)

32.72 P. Siedle, H.-J. Butt, E. Bamberg, D. N. Wang, W. Kuhlbrandt, J. Zach, M. Haider: Determining the form of atomic force microscope tips. In: *X-Ray Optics and Microanalysis 1992*, Proceedings of the Thirteenth International Congress, Manchester, UK, ed. by P. B. Kenway, P. J. Duke, G. W. Lorimer, T. Mulvey, J. W. Drummond, G. Love, A. G. Michette, M. Stedman (IOP, Bristol 1992)

32.73 S. Xu, M. F. Arnsdorf: Calibration of the scanning (atomic) force microscope with gold particles, J. Microsc. **3**, 199–210 (1994)

32.74 U. D. Schwarz, O. Zwörner, P. Köster, R. Wiesendanger: Friction force spectroscopy in the low-load regime with well-defined tips. In: *Micro/Nanotribology and Its Applications*, ed. by B. Bhushan (Kluwer, Dordrecht 1997)

32.75 S. J. O'shea, R. N. Atta, M. E. Welland: Characterization of tips for conducting atomic force microscopy, Rev. Sci. Instrum. **66**, 2508–2512 (1995)

32.76 P. Niedermann, W. Hanni, N. Blanc, R. Christoph, J. Burger: Chemical vapor deposition diamond for tips in nanoprobe experiments, J. Vacuum Sci. Technol. A **14**, 1233–1236 (1995)

32.77 L. M. Qian, X. D. Xiao, S. Z. Wen: Tip in situ chemical modification and its effects on tribological measurements, Langmuir **16**, 662–670 (2000)

32.78 E. L. Florin, V. T. Moy, H. E. Gaub: Adhesion forces between individual ligand–receptor pairs, Science **264**, 415–417 (1994)

32.79 V. T. Moy, E. L. Florin, H. E. Gaub: Intermolecular forces and energies between ligands and receptors, Science **266**, 257–259 (1994)

32.80 G. U. Lee, L. A. Chrisey, R. J. Colton: Direct measurement of the forces between complementary strands of DNA, Science **266**, 771–773 (1994)

32.81 S. S. Wong, E. Joselevich, A. T. Woolley, C. Chin Li, C. M. Lieber: Covalently functionalized nanotubes as nanometre-sized probes in chemistry and biology, Nature **394**, 52–55 (1998)

32.82 O. H. Willemsen, M. M. E. Snel, K. O. Van Der Werf, B. G. De Grooth, J. Greve, P. Hinterdorfer, H. J. Gruber, H. Schindler, Y. Van Kooyk, C. G. Figdor: Simultaneous height and adhesion imaging of antibody-antigen interactions by atomic force microscopy, Biophys. J. **75**, 2220–2228 (1998)

32.83 W. A. Ducker, T. J. Senden, R. M. Pashley: Direct measurement of colloidal forces using an atomic force microscope, Nature **353**, 239–241 (1991)

32.84 H. J. Butt: Measuring electrostatic, van der Waals, and hydration forces in electrolyte solutions with an atomic force microscope, Biophys. J. **60**, 1438–1444 (1991)

32.85 V. S. J. Craig, C. Neto: In situ calibration of colloid probe cantilevers in force microscopy: hydrodynamic drag on a sphere approaching a wall, Langmuir **17**, 6018–6022 (2001)

32.86 R. J. Cannara, M. J. Brukman, R. W. Carpick: Cantilever tilt compensation for variable-load atomic force microscopy, Rev. Sci. Instrum. **76**, 53706 (2005)

32.87 R. Staub, D. Alliata, C. Nicolini: Drift elimination in the calibration of scanning probe microscopes, Rev. Sci. Instrum. **66**, 2513–2516 (1995)

32.88 S. M. Hues, C. F. Draper, K. P. Lee, R. J. Colton: Effect of PZT and PMN actuator hysteresis and creep on nanoindentation measurements using force microscopy, Rev. Sci. Instrum. **65**, 1561–1565 (1994)

32.89 J. Fu: In situ testing and calibrating of z-piezo of an atomic force microscope, Rev. Sci. Instrum. **66**, 3785–3788 (1995)

32.90 J. Garnaes, L. Nielsen, K. Dirscherl, J. F. Jorgensen, J. B. Rasmussen, P. E. Lindelof, C. B. Sorensen: Two-dimensional nanometer-scale calibration based on one-dimensional gratings, Appl. Phys. A **66**, 831–5 (1998)

32.91 J. F. Jorgensen, K. Carneiro, L. L. Madsen, K. Conradsen: Hysteresis correction of scanning tunneling microscope images, J. Vacuum Sci. Technol. B **1**, 1702–1704 (1994)

32.92 J. F. Jorgensen, L. L. Madsen, J. Garnaes, K. Carneiro, K. Schaumburg: Calibration, drift elimination, and molecular structure analysis, J. Vacuum Sci. Technol. B **12**, 1698–1701 (1994)

32.93 M. Jaschke, H.J. Butt: Height calibration of optical lever atomic force microscopes by simple laser interferometry, Rev. Sci. Instrum. **66**, 1258–1259 (1995)

32.94 L.A. Nagahara, K. Hashimoto, A. Fujishima, D. Snowden-Ifft, P.B. Price: Mica etch pits as a height calibration source for atomic force microscopy, J. Vacuum Sci. Technol. B **12**, 1694–7 (1993)

32.95 H.M. Brodowsky, U.-C. Boehnke, F. Kremer: Wide range standard for scanning probe microscopy height calibration, Rev. Sci. Instrum. **67**, 4198–4200 (1996)

32.96 R.M. Overney, H. Takano, M. Fujihira: Elastic compliances measured by atomic force microscopy, Europhys. Lett. **26**, 443–447 (1994)

32.97 M.S. Marcus, R.W. Carpick, D.Y. Sasaki, M.A. Eriksson: Material anisotropy revealed by phase contrast in intermittent contact atomic force microscopy, Phys. Rev. Lett. **88**, 226103 (2002)

32.98 M.J. D'amato, M.S. Marcus, M.A. Eriksson, R.W. Carpick: Phase imaging and the lever-sample tilt angle in dynamic atomic force microscopy, Appl. Phys. Lett. **85**, 4378–4380 (2004)

32.99 L.-O. Heim, M. Kappl, H.-J. Butt: Tilt of atomic force microscope cantilevers: Effect on spring constant and adhesion measurements, Langmuir **20**, 2760–2764 (2004)

32.100 J.L. Hutter: Comment on tilt of atomic force microscope cantilevers: Effect on spring constant and adhesion measurements, Langmuir **21**, 2630–2632 (2005)

32.101 P.G. De Gennes: Wetting: statistics and dynamics, Rev. Mod. Phys. **57**, 827–863 (1985)

32.102 T. Stifter, O. Marti, B. Bhushan: Theoretical investigation of the distance dependence of capillary and van der Waals forces in scanning force microscopy, Phys. Rev. B **62**, 13667–13673 (2000)

32.103 Y. Sugawara, M. Ohta, T. Konishi, S. Morita, M. Suzuki, Y. Enomoto: Effects of humidity and tip radius on the adhesive force measured with atomic force microscopy, Wear **168**, 13–16 (1993)

32.104 M. Binggeli, C.M. Mate: Influence of capillary condensation of water on nanotribology studied by force microscopy, Appl. Phys. Lett. **65**, 415–417 (1994)

32.105 X. Xiao, Q. Linmao: Investigation of humidity-dependent capillary force, Langmuir **16**, 8153–8158 (2000)

32.106 F.M. Orr, L.E. Scriven, A.P. Rivas: Pendular rings between solids: meniscus properties and capillary force, J. Fluid Mech. **67**, 723–742 (1975)

32.107 H.K. Christenson: Adhesion between surfaces in undersaturated vapors – a re-examination of the influence of meniscus curvature and surface forces, J. Colloid Interf. Sci. **121**, 170–178 (1988)

32.108 E. Riedo, F. Levy, H. Brune: Kinetics of capillary condensation in nanoscopic sliding friction, Phys. Rev. Lett. **88**, 185505/1–4 (2002)

32.109 D. Maugis, B. Gauthiermanuel: JKR–DMT transition in the presence of a liquid meniscus, J. Adhes. Sci. Technol. **8**, 1311–1322 (1994)

32.110 A. Fogden, L.R. White: Contact elasticity in the presence of capillary condensation. 1. The non-adhesive Hertz problem, J. Colloid Interf. Sci. **138**, 414–430 (1990)

32.111 K.L. Johnson, K. Kendall, A.D. Roberts: Surface energy and the contact of elastic solids, Proc. R. Soc. Lond. A **324**, 301–313 (1971)

32.112 K.L. Johnson: Adhesion and friction between a smooth elastic asperity and a plane surface, Proc. R. Soc. Lond. A **453**, 163–179 (1997)

32.113 K. Johnson, J. Greenwood: An adhesion map for the contact of elastic spheres, J. Colloid Interf. Sci. **192**, 326–333 (1997)

32.114 T. Thundat, X.Y. Zheng, G.Y. Chen, R.J. Warmack: Role of relative humidity in atomic force microscopy imaging, Surf. Sci. **294**, L939–L943 (1993)

32.115 M. Binggeli, R. Christoph, H.-E. Hintermann: Observation of controlled, electrochemically induced friction force modulations in the nano-Newton range, Tribol. Lett. **1**, 13–21 (1995)

32.116 B. Bhushan, S. Sundararajan: Micro/nanoscale friction and wear mechanisms of thin films using atomic force and friction force microscopy, Acta Mater. **46**, 3793–3804 (1998)

32.117 W. Gulbinski, D. Pailharey, T. Suszko, Y. Mathey: Study of the influence of adsorbed water on AFM friction measurements on molybdenum trioxide thin films, Surf. Sci. **475**, 149–158 (2001)

32.118 M. He, A.S. Blum, D.E. Aston, C. Buenviaje, R.M. Overney, R. Luginbuhl: Critical phenomena of water bridges in nanoasperity contacts, J. Chem. Phys. **114**, 1355–1360 (2001)

32.119 A.W. Adamson: *Physical Chemistry of Surfaces*, 5th edn. (Wiley, 1990) Chap. 16, pp. 591–615

32.120 C.M. Mate: Application of disjoining and capillary pressure to liquid lubricant films in magnetic recording, J. Appl. Phys. **72**(2), 3084–3090 (1992)

32.121 C. Gao: Theory of menisci and its applications, Appl. Phys. Lett. **71**(13), 1801–1803 (1997)

32.122 G. Lian, C. Thornton, M.J. Adams: A theoretical study of the liquid bridge forces between two rigid spherical bodies, J. Colloid Interf. Sci. **161**, 138–147 (1993)

32.123 C.D. Willett, M.J. Adams, S.A. Johnson, J.P.K. Seville: Capillary bridges between two spherical bodies, Langmuir **16**, 9396–9405 (2000)

32.124 J.A. Greenwood, J.B.P. Williamson: Contact of nominally flat surfaces, Proc. R. Soc. Lond. A **295**, 300–319 (1966)

32.125 R. Maboudian: Surface processes in MEMS technology, Surf. Sci. Rep. **30**, 207–270 (1998)

32.126 R. Maboudian, W.R. Ashurst, C. Carraro: Self-assembled monolayers as anti-stiction coatings for MEMS: Characteristics and recent developments, Sensors Actuat. A **82**, 219–223 (2000)

32.127 R. Maboudian, W. R. Ashurst, C. Carraro: Tribological challenges in micromechanical systems, Tribol. Lett. **12**, 95–100 (2002)

32.128 K. Komvopoulous: Surface engineering and microtribology for microelectromechanical systems, Wear **200**, 305–327 (1996)

32.129 A. Noy, D. V. Vezenov, C. M. Lieber: Chemical force microscopy, Annu. Rev. Mater. Sci **27**, 381–421 (1997)

32.130 H. Takano, J. R. Kenseth, S.-S. Wong, J. C. O'brien, M. D. Porter: Chemical and biochemical analysis using scanning force microscopy, Chem. Rev. **99**, 2845–2890 (1999)

32.131 D. L. Sedin, K. L. Rowlen: Adhesion forces measured by atomic force microscopy in humid air, Anal. Chem. **72**, 2183–2189 (2000)

32.132 T. Han, J. M. Williams, T. P. Beebe: Chemical bonds studied with functionalized atomic force microscopy tips, Anal. Chim. Acta **307**, 365–376 (1995)

32.133 L. A. Wenzler, G. L. Moyes, L. G. Olson, J. M. Harris, T. P. Beebe: Single-molecule bond rupture force analysis of interactions between AFM tips and substrates modified with organosilanes, Anal. Chem. **69**, 2855–2861 (1997)

32.134 L. A. Wenzler, G. L. Moyes, G. N. Raikar, R. L. Hansen, J. M. Harris, T. P. B.. Jr: Measurements of single-molecule bond rupture forces between self-assembled monolayers of organosilanes with the atomic force microscope, Langmuir **13**, 3761–3768 (1997)

32.135 C. D. Frisbie, L. F. Rozsnyai, A. Noy, M. S. Wrighton, C. M. Lieber: Functional group imaging by chemical force microscopy, Science **265**, 2071–2074 (1994)

32.136 A. Noy, C. D. Frisbie, L. F. Rozsnyai, M. S. Wrighton, C. M. Lieber: Chemical force microscopy: Exploiting chemically-modified tips to quantify adhesion, friction and functional group distributions in molecular assemblies, J. Am. Chem. Soc. **117**, 7943–7951 (1995)

32.137 D. V. Vezenov, A. Noy, L. F. Rozsnyai, C. M. Lieber: Force titrations, ionization state sensitive imaging of functional group distributions in molecular assemblies, J. Am. Chem. Soc. **119**, 2006–2015 (1997)

32.138 S. S. Wong, A. T. Woolley, E. Joselevich, C. L. Cheung, C. M. Lieber: Covalently-functionalized single-walled carbon nanotube tips for chemical force microscopy, J. Am. Chem. Soc. **120**, 8557–8558 (1998)

32.139 D. V. Vezenov, A. V. Zhuk, G. M. Whitesides, C. M. Likeber: Chemical force spectroscopy in heterogeneous systems: Intermolecular interactions involving epoxy polymer, mixed monolayers and polar solvents, J. Am. Chem. Soc. **124**, 10578–10588 (2002)

32.140 J. E. Houston, H. I. Kim: Adhesion, friction, and mechanical properties of functionalized alkanethiol self-assembled monolayers, Acc. Chem. Res. **35**, 547–553 (2002)

32.141 T. Ito, M. Namba, P. Buhlmann, Y. Umezawa: Modification of silicon nitride tips with trichlorosilane self-assembled monolayers (SAMs) for chemical force microscopy, Langmuir **13**, 4323–4332 (1997)

32.142 H. I. Kim, M. Graupe, O. Oloba, T. Koini, S. Imaduddin, T. R. Lee, S. S. Perry: Molecularly specific studies of the frictional properties of monolayer films: A systematic comparison of CF_3-, (CH3) (32.2) CH-, CH_3-terminated films, Langmuir **15**, 3179–3185 (1999)

32.143 H. I. Kim, J. E. Houston: Separating mechanical and chemical contributions to molecular-level friction, J. Am. Chem. Soc. **122**, 12045–12046 (2000)

32.144 S. Lee, Y. S. Shon, R. Colorado, R. L. Guenard, T. R. Lee, S. S. Perry: The influence of packing densities and surface order on the frictional properties of alkanethiol self-assembled monolayers (SAMs) on gold: A comparison of SAMs derived from normal and spiroalkanedithiols, Langmuir **16**, 2220–2224 (2000)

32.145 Y. Leng, S. Jiang: Dynamic simulations of adhesion and friction in chemical force microscopy, J. Am. Chem. Soc. **124**, 11764–11770 (2002)

32.146 T. Nakagawa, K. Ogawa, T. Kurumizawa: Discriminating molecular length of chemically adsorbed molecules using an atomic force microscope having a tip covered with sensor molecules (an atomic force microscope having chemical sensing function), Jpn. J. Appl. Phys. **32**, 294–296 (1993)

32.147 T. Nakagawa, K. Ogawa, T. Kurumizawa: Atomic force microscope for chemical sensing, J. Vacuum Sci. Tech. B **12**, 2215–2218 (1994)

32.148 S. K. Sinniah, A. B. Steel, C. J. Miller, J. E. Reutt-Robey: Solvent exclusion and chemical contrast in scanning force microscopy, J. Am. Chem. Soc. **118**, 8925–8931 (1996)

32.149 H. Skulason, C. D. Frisbie: Detection of discrete interactiuons upon rupture of Au microcontacts to self-assembled monolayers terminated with $-S(CO)CH_3$ or $-SH$, J. Am. Chem. Soc. **122**, 9750–9760 (2000)

32.150 E. W. V. D. Vegte, G. Hadziioannou: Scanning force microscopy with chemical specificity: An extensive study of chemically specific tip–surface interactions and the chemical imaging of surface functional groups, Langmuir **13**, 4357–4368 (1997)

32.151 V. Tsukruk, V. N. Bliznyuk: Adhesive and friction forces between chemically modified silicon and silicon nitride surfaces, Langmuir **14**, 446–455 (1998)

32.152 E. W. V. D. Vegte, G. Hadziioannou: Acid-base properties and the chemical imaging of surface-bound functional groups with scanning force microscopy, J. Phys. Chem. B **101**, 9563–9569 (1997)

32.153 J. Zhang, J. Kirkham, C. Robinson, M. L. Wallwork, D. A. Smith, A. Marsh, M. Wong: Determination of the ionization state of 11-thioundecyl-1-phosphonic acid in self-assembled monolayers by

chemical force microscopy, Anal. Chem. **72**, 1973–1978 (2000)
32.154 B. Xu, X. Xiao, N.J. Tao: Measurements of single-molecule electromechanical properties, J. Am. Chem. Soc. **125**, 16164–16165 (2003)
32.155 A. Lio, C. Morant, D.F. Ogletree, M. Salmeron: Atomic force microscopy study of the pressure-dependent structural and frictional properties of n-alkanethiols on gold, J. Phys. Chem. B **101**, 4767–4773 (1997)
32.156 S.-S. Wong, H. Takano, M.D. Porter: Mapping orientation differences of terminal functional groups by friction force microscopy, Anal. Chem. **70**, 5209–5212 (1998)
32.157 A. Lio, D.H. Charych, M. Salmeron: Comparative atomic force microscopy study of the chain length dependence of frictional properties of alkanethiols on gold and alkysilanes on mica, J. Phys. Chem. B **101**, 3800–3805 (1997)
32.158 X. Xiao, J. Hu, D.H. Charych, M. Salmeron: Chain length dependence of the frictional properties of alkylsilane molecules self-assembled on mica studied by atomic force microscopy, Langmuir **12**, 235–237 (1996)
32.159 G.-Y. Liu, M. Salmeron: Reversible displacement of chemisorbed n-alkane thiol molecules on Au(111) surface: An atomic force microscopy study, Langmuir **10**, 367–370 (1994)
32.160 A.B. Tutein, S.J. Stuart, J.A. Harrison: Indentation analysis of linear-chain hydrocarbon monolayers anchored to diamond, J. Phys. Chem. B **103**, 11357–11365 (1999)
32.161 R.L. Pizzolatto, Y.J. Yang, L.K. Wolf, M.C. Messmer: Conformational aspects of modal chromatographic surfaces studied by sum-frequency generation, Anal. Chem. Acta **397**, 81–92 (1999)
32.162 E.W.V.D. Vegte, A. Subbotin, G. Hadziioannou: Nanotribological properties of unsymmetrical n-dialkyl sulfide monolayers on gold: Effect of chain length on adhesion, friction and imaging, Langmuir **16**, 3249–3256 (2000)
32.163 Y.-S. Lo, J. Simons, T.P.B. Jr: Temperature dependence of the biotin–avidin bond rupture force studied by atomic force microscopy, J. Phys. Chem. B **106**, 9847–9857 (2002)
32.164 Y.-S. Lo, N.D. Huefner, W.S. Chan, F. Stevebs, J.M. Harris, J.T.P. Beebe: Specific interactions between biotin and avidin studies by atomic force microscopy using the Poisson statistical analysis method, Langmuir **15**, 1373–1382 (1999)
32.165 J.H. Hoh, J.P. Cleavland, C.B. Prater, J.-P. Revel, P.K. Hansma: Quantitized adhesion detected with the atomic force microscope, J. Am. Chem. Soc. **114**, 4917–4918 (1992)
32.166 M. Grandbois, M. Beyer, M. Rief, H. Clausen-Schaumann, H.E. Gaub: How strong is a covalent bond?, Science **283**, 1727–1730 (1999)
32.167 H. Skulason, C.D. Frisbie: Contact mechanics modeling of pull-off measurements: Effect of solvent, probe radius, and chemical binding probability on the detection of single-bond rupture forces by atomic force microscopy, Anal. Chem. **74**, 3096–3104 (2002)
32.168 H. Schonherr, V. Chechik, C.J.M. Stirling, G.J. Vancso: Monitoring surface reactions at an AFM tip: An approach to following reaction kinetics in self-assembled monolayers on the nanometer scale, J. Am. Chem. Soc. **122**, 3679–3687 (2000)
32.169 M.P.L. Werts, E.W.V.D. Vegte, G. Hadziioannou: Surface chemical reactions probed with scanning force microscopy, Langmuir **13**, 4939–4942 (1997)